Fully coupled material response and internal radiative heat transfer for 3D heat shield modeling

Raghava S. C. Davuluri * and Rui Fu† and Kaveh A. Tagavi ‡ and Alexandre Martin §¶
University of Kentucky, Lexington, KY, 40506, USA

A material response code is strongly coupled with a radiative transfer equation (RTE) to evaluate the effect of a spectrally resolved heat flux on the thermal response of a heat shield. A P_1 approximation model of RTE is used to account for radiation heat transfer within the material. First, the RTE model is verified by comparing the numerical results with the analytical solution. Next, the coupling scheme is verified by comparing the temperature histories computed by the pure conduction scheme with the ones computed by conduction coupled with radiative emission. The verification study is conducted using test cases from the literature (radiant heating, arc-jet heating, and space shuttle entry) as well as on a 3D Block, a 2D IsoQ sample, and the Stardust Return Capsule. The verification results are satisfactory for all cases. Thus, the verification results indicate that the coupling approach can accurately simulate the thermal response of the material. The coupling scheme was then used to simulate a laser heating experiment that studied the impact of spectral radiative heat transfer on ablative material. The results from the laser ablation simulations exhibit a behavior analogous to the experimental observations, indicating the importance of spectral radiative flux on the material response.

Nomenclature

Symbols

c	Speed of sound, m/s
c_p	Specific heat, J/kg-K
$\mathbf{D}$	Diffusive momentum source term, (D_x, D_y, D_z), kg/m-s^2
E	Total energy per unit volume, J/m^3
$\mathbf{F}_{\text{cond}}$	Conduction heat flux, $(F_{\text{cond},x}, F_{\text{cond},y}, F_{\text{cond},z})$, W/m^2
$\mathcal{F}$	Convective flux matrix
$\mathcal{F}_d$	Diffusive flux matrix
G_λ	Spectral incident radiation flux, W/m^2-μm
H	Specific enthalpy, J/kg
I_λ	Spectral intensity, W/m^2-μm-sr
$I_{b\lambda}$	Planck function, W/m^2-μm-sr
k	Thermal conductivity, W/m-K
M	Order of approximation for phase function
$\hat{\mathbf{n}}$	Unit normal vector
p	Static pressure, N/m^2
P	Legendre Polynomials
$\mathbf{q}_\lambda$	Spectral radiative flux, W/m^2-μm
$\mathbf{q}_{\text{rad}}$	Total radiative flux, W/m^2
$\mathbf{Q}$	Conservative variables vector
$\mathbf{S}$	Source term vector

*Graduate Research Assistant, Mechanical and Aerospace Engineering, Student Member AIAA
†Research Scientist, Mechanical and Aerospace Engineering, Member AIAA
‡Professor, Mechanical and Aerospace Engineering
§Professor, Mechanical and Aerospace Engineering, 261 Ralph G Anderson Building, Associate Fellow AIAA
¶Presented as Paper 2021-3131 at the AIAA Aviation 2021 Forum, Virtual Event, August 2-6, 2021.

$\hat{\mathbf{s}}$	Directional unit vector
S_D	Diffusive energy source term, W/m^3
t	Time, s
T	Temperature, K
ΔT	Temperature difference, K
(u, v, w)	Velocity components, m/s
Y	Spherical harmonics
β	Extinction coefficient, $(\kappa + \sigma_s)$, 1/m
ϵ	Emissivity
θ	Polar angle, rad
κ	Absorption coefficient, 1/m
ρ	Density, kg/m^3
σ_s	Scattering coefficient, 1/m
ϕ	Porosity
ϕ_s	Scattering phase function
ψ	Azimuthal angle, rad
Ω	Solid angle, sr
$\dot{\omega}_{g_i}$	Pyrolysis gas production rate for gas species i, kg/m^3-s
$\dot{\omega}_{s_i}$	Decomposition rate for solid species i, kg/m^3-s

Subscripts

eff	Effective
g	Gas
s	Solid
$s + g$	Solid + Gas
λ	Spectral

I. Introduction

Space vehicles enter the planetary atmosphere at hypersonic speeds and experience high surface heat fluxes. The high enthalpy of the flow contributes to the convective heat flux and shock layer emissions to the radiative heat flux. These vehicles are equipped with Thermal Protection System (TPS) that counter these high heat fluxes and protect the vehicle from extreme conditions. For most vehicles of interest to NASA, ablative materials are used as TPS, which undergo mass removal mechanisms to absorb the intense heat [1].

The heat transfer process for ablative materials involves different mechanisms. For a simple non-reactive fibrous material, the energy transit occurs in the form of heat conduction through the solid and gas and internal radiation through the porous structure. Several studies [2–4] indicate that internal radiation is significant and, in some cases, is the dominant mode of heat transfer, which contributes to volumetric ablation. The thermal response of the material is numerically modeled using Material Response (MR) codes. These codes use the parameter *effective* thermal conductivity that accounts for both heat conduction and internal radiation [2, 5].

It is generally assumed that the radiative flux, incident on the surface, is either reflected or absorbed within a minute thickness near the surface of the material. The experiments by White [6], who used a solar tower to irradiate Phenolic Impregnated Carbon Ablator (PICA) samples with incident flux levels at 50, 100, 150 W/cm^2, indicated no in-depth transmission and absorption in the near-infrared wavelength range of radiative heating. However, recently, the assumption proved to be invalid when White [7] conducted laser testing on silica, glass-fiber, and carbon-felt-based materials. White [7] used two types of lasers – CO_2 laser (wavelength = 10.6 μm) and Fiber laser (wavelength = 1.07 μm) – both imposing a heat flux of 115 W/cm^2 on the samples for 30 seconds. When the two lasers irradiated the samples of the same material, it was found that the material response was quite different. The values for the parameters such as mass loss, char layer thickness, maximum bondline temperature, and time to reach maximum bondline temperature

were higher for the sample irradiated by the Fiber laser when compared to the CO_2 laser. The results indicated that the spectral radiation penetrates through a significant depth of the material and impacts the material response. Since the shock layer radiation can be expressed through narrow bands of emission [8], it is important to account for the effects of spectral radiative flux to define the performance of TPS accurately.

The *effective* thermal conductivity takes into account only total radiative heat flux and does not consider its spectral contribution. Therefore, to compute the material response to a spectral radiative flux, the heat conduction and internal radiation should be solved separately and later coupled to ensure total heat transfer is modeled accurately.

In this work, a P_1 approximation model [9] of the Radiation Transfer Equation (RTE) is used to compute the internal radiation. The objective of the present work is to showcase the functionality of the developed tool by performing verification for cases of multi-dimensional models and simulating the laser ablation to understand the significance of spectral radiation within a material. The present work is an extension to work performed by Martin and Panesi [10].

II. Numerical Approach

A material response code is used to compute the heat conduction through the material and its solid decomposition. On the other hand, the internal radiative heat transfer is solved by using P_1 approximation model for the radiative transfer equation. Individual models and the coupling procedure are presented in this section.

A. Material Response

The material response is simulated using the MR module of KATS (Kentucky Aerothermodynamics and Thermal-response System) [11–13]. The solver employs a finite volume method applied to the governing equations, which are of the form:

$$\frac{\partial \mathbf{Q}}{\partial t} + \nabla \cdot (\boldsymbol{\mathcal{F}} - \boldsymbol{\mathcal{F}_d}) = \mathbf{S} \quad , \tag{1}$$

where $\mathbf{Q}$ is a vector of conservative variables; $\boldsymbol{\mathcal{F}}$ and $\boldsymbol{\mathcal{F}_d}$ are convective and diffusive flux matrices; and $\mathbf{S}$ is the source term vector. The vectors of conservative variables and source terms are of the form:

$$\mathbf{Q} = \begin{pmatrix} \phi\rho_{g_1} \\ \vdots \\ \phi\rho_{g_{ngs}} \\ \rho_{s_1} \\ \vdots \\ \rho_{s_{nss}} \\ \phi\rho_g u \\ \phi\rho_g v \\ \phi\rho_g w \\ \phi E_g + E_s \end{pmatrix}, \qquad \mathbf{S} = \begin{pmatrix} \dot{\omega}_{g_1} \\ \vdots \\ \dot{\omega}_{g_{ngs}} \\ \dot{\omega}_{s_1} \\ \vdots \\ \dot{\omega}_{s_{nss}} \\ D_x \\ D_y \\ D_z \\ S_D \end{pmatrix}, \tag{2}$$

where ϕ is the porosity of the material, ρ is the density, (u, v, w) are the components of gas velocity, E is the total energy per unit volume. (D_x, D_y, D_z) are terms that account for the diffusive effects of porous structure in the momentum equation, S_D is the diffusive source in the energy equation, $\dot{\omega}_{g_i}$ is the rate of mass production of pyrolysis gas species 'i', and $\dot{\omega}_{s_i}$ is the mass decomposition rate of solid species 'i'. Subscripts ngs and nss represent the total number of gas and solid species, respectively, while g and s represent the gas and solid states. The convective and diffusive flux matrices in Eq. (1) are given as:

$$\boldsymbol{\mathcal{F}} = \begin{pmatrix} \phi\rho_{g_1}u & \phi\rho_{g_1}v & \phi\rho_{g_1}w \\ \vdots & \vdots & \vdots \\ \phi\rho_{g_{ngs}}u & \phi\rho_{g_{ngs}}v & \phi\rho_{g_{ngs}}w \\ 0 & 0 & 0 \\ \vdots & \vdots & \vdots \\ 0 & 0 & 0 \\ \phi\rho_g u^2 + p & \phi\rho_g vu & \phi\rho_g wu \\ \phi\rho_g uv & \phi\rho_g v^2 + p & \phi\rho_g wv \\ \phi\rho_g uw & \phi\rho_g vw & \phi\rho_g w^2 + p \\ \phi\rho_g uH & \phi\rho_g vH & \phi\rho_g wH \end{pmatrix}, \qquad \boldsymbol{\mathcal{F}_d} = \begin{pmatrix} & 0 & \\ & & \\ & & \\ & & \\ & & \\ F_{\text{cond},x} & F_{\text{cond},y} & F_{\text{cond},z} \end{pmatrix} \tag{3}$$

where p is the static pressure, H is the specific gas enthalpy, and $F_{\text{cond},i}$ are the conductive heat flux components. Eq. (1) is discretized first-order in time and second-order in space. The solver uses the PETSc library [14–16] to solve the linear system of equations, ParMETIS [17] for domain decomposition, and MPI [18] for message passing. More information on this solver is presented in the works by Weng et al. [11, 19, 20].

B. Radiation Transfer Equation

The radiative energy balance in participating media (absorbing, emitting, and scattering media) is given by the Radiative Transfer Equation (RTE) [9]. RTE indicates the radiation intensity field within the enclosures as a function of location, direction, and wavelength and is written as:

$$\frac{1}{c}\frac{\partial I_\lambda}{\partial t} + \hat{\mathbf{s}} \cdot \nabla I_{b\lambda} = \kappa_\lambda I_{b\lambda} - (\kappa_\lambda + \sigma_{s\lambda})\, I_\lambda + \frac{\sigma_{s\lambda}}{4\pi} \int_{4\pi} I_\lambda\left(\hat{\mathbf{s}}_i\right) \phi_{s\lambda}\left(\hat{\mathbf{s}}_i, \hat{\mathbf{s}}\right) d\Omega_i \tag{4}$$

where $\hat{\mathbf{s}}$ is the directional unit vector, I_λ is the spectral intensity, $I_{b\lambda}$ is the Planck function, κ_λ is the spectral absorption coefficient, $\sigma_{s\lambda}$ is the spectral scattering coefficient, $\phi_{s\lambda}\left(\hat{\mathbf{s}}_i, \hat{\mathbf{s}}\right)$ is the scattering phase function, c is the speed of light, Ω is the solid angle, and subscript i is the direction of an incoming ray. For most of the applications, the first term of Eq. (4) is minimal and can be neglected [9]. Therefore, Eq. (4) can be re-written as

$$\hat{\mathbf{s}} \cdot \nabla I_{b\lambda} = \frac{dI_\lambda}{ds} = \kappa_\lambda I_{b\lambda} - \beta_\lambda I_\lambda + \frac{\sigma_{s\lambda}}{4\pi} \int_{4\pi} I_\lambda\left(\hat{\mathbf{s}}_i\right) \phi_{s\lambda}\left(\hat{\mathbf{s}}_i, \hat{\mathbf{s}}\right) d\Omega_i \tag{5}$$

where β_λ is the spectral extinction coefficient, which is equal to the sum of spectral absorption and spectral scattering coefficients. Solving Eq. (5) is challenging due to its directional nature, even for 1D cases.

Methods such as Spherical Harmonics (P_N), Discrete-Ordinates (S_N), Monte-Carlo, and Zonal are used to solve Eq. (5) providing approximate solutions [9]. The Spherical Harmonics (P_N) method converts Eq. (5) into a set of simultaneous partial differential equations (PDE). The P_N method expresses the radiation intensity field, I, in terms of orthogonal-basis functions in spherical coordinate system [21]. In the P_N method, $I(r, \hat{\mathbf{s}})$ at any location r is assumed to be the sum of the value of a scalar function on the surface of a sphere of unit length radius around point r. This scalar function is expressed as

$$I(r, \hat{\mathbf{s}}) = \sum_{l=0}^{\infty} \sum_{m=-l}^{l} I_l^m(r) Y_l^m(\hat{\mathbf{s}}) \tag{6}$$

where $I_l^m(r)$ are coefficients based on the position and $Y_l^m(\hat{\mathbf{s}})$ are spherical harmonics which are defined as

$$Y_l^m(\hat{\mathbf{s}}) = (-1)^{(m+|m|)/2} \left[\frac{(l-|m|)!}{(l+|m|)!}\right]^{1/2} e^{im\psi} P_l^{|m|}(\cos\theta) \tag{7}$$

where θ and ψ are polar and azimuthal angles defining the direction unit vector $\hat{\mathbf{s}}$, and P_l^m are associated with Legendre Polynomials. The scattering function is also expressed in the form of Legendre Polynomials as

$$\phi_s\left(\hat{\mathbf{s}}_i, \hat{\mathbf{s}}\right) = \sum_{m=0}^{M} A_m P_m\left(\hat{\mathbf{s}}_i\right) P_m\left(\hat{\mathbf{s}}\right) \tag{8}$$

where M is the order of approximation for the phase function. The P_1 approximation to the RTE is obtained when the terms in Eq. (6) is calculated for $l = 1$. The resulting PDE is a function of variable G, which is the total intensity acting on a point from all directions and is defined as:

$$G(r) = \int_{4\pi} I(r, \hat{\mathbf{s}}) d\Omega \tag{9}$$

Applying the P_1 approximation to Eq. (5) results in

$$\nabla \cdot \mathbf{q}_\lambda = \kappa_\lambda \left(4\pi I_{b\lambda} - G_\lambda\right) \tag{10}$$

where $\mathbf{q}_\lambda$ represent spectral radiative heat flux and is defined as

$$\mathbf{q}_\lambda(r) = \int_{4\pi} I(r, \hat{\mathbf{s}}) \hat{\mathbf{s}} d\Omega \tag{11}$$

Additionally, multiplying Eq. (10) by Y_l^m results in new relation as

$$\nabla G_\lambda = -3\beta_\lambda \mathbf{q}_\lambda \tag{12}$$

A *Helmholtz* equation is formed by eliminating spectral heat flux from Eqs. (10) and (12) that results in:

$$\nabla \cdot \left(-\frac{1}{3\beta_\lambda} \nabla G_\lambda\right) = \kappa_\lambda \left(4\pi I_{b\lambda} - G_\lambda\right) \tag{13}$$

The above equation is solved for G_λ. It should be noted that Eq. (13) is a second-order elliptic PDE that is straightforward to integrate and less complicated when compared to other approximate methods. The P_1 method can be applied to scattering media but is less accurate when the medium is optically thin [9, 21]. Finally, a Marshak boundary condition [22, 23] is applied for the RTE at boundaries:

$$\mathbf{q}_\lambda \cdot \hat{\mathbf{n}} = \frac{\epsilon}{2\left(2 - \epsilon\right)} \left(4\pi I_{b\lambda} - G_\lambda\right) \tag{14}$$

where $\hat{\mathbf{n}}$ represents the normal vector and ϵ represents the emissivity of the material.

C. Solution Procedure

The general form of the energy equation from Eq. (1) for heat conduction is given as:

$$\rho_s c_p \frac{\partial T}{\partial t} = \nabla \cdot k_{\text{eff}} \nabla T \tag{15}$$

where ρ_s is the bulk solid density of the material, c_p is specific heat capacity of solid, T is the temperature, t is time, and k_{eff} is the *effective* thermal conductivity. The heat conduction through the solid material solved by using Eq. (15) is referred as "**pure conduction**" in this work. The *effective* thermal conductivity takes into account the thermal conductivities of solid, gas, as well as radiation. However, the values of k_{eff} are accurate in an optically thick and isotropic medium, where the approximations leading to radiative conductivity are valid [24–26]. Though the approximation of optically thick medium stands valid, the medium's isotropic nature assumption does not stand true at large temperature gradients [27, 28]. The most common situations where large temperature gradients occur are during arc-jet and radiant heating tests. Also, the value of k_{eff}, especially for low-density ablators, is often under-predicted

through suppressing the radiation energy transport by scattering and absorption [29]. Therefore, a coupled approach between heat conduction and RTE is used. Also, pure conduction only accounts for the effect of total radiative heat transfer, whereas the coupled approach can also be used to simulate the effect of spectral radiative heat transfer on the material response. The energy equation for the coupled approach is of the form:

$$\rho_s c_p \frac{\partial T}{\partial t} = \nabla \cdot \left(k_{s+g} \nabla T + \mathbf{q}_{\text{rad}}\right) = \nabla \cdot \left(k_{s+g} \nabla T\right) + \nabla \cdot \mathbf{q}_{\text{rad}} \tag{16}$$

where k_{s+g} is the thermal conductivity that takes into account the contributions of solid and gas phase, and $\mathbf{q}_{\text{rad}}$ is the total radiative heat flux through the solid. The heat conduction through the solid material solved by using Eq. (16) is referred as "**conduction coupled with radiative emission**" in this work. It can be seen that Eq. (16) when compared to Eq. (15), has an additional term. The extra term $\nabla \cdot \mathbf{q}_{\text{rad}}$ is added into source term vector $\mathbf{S}$ of Eq. (1). The total radiative flux is determined as

$$\nabla \cdot \mathbf{q}_{\text{rad}} = \int_{\lambda} \nabla \cdot \mathbf{q}_{\lambda} d\lambda = \int_{\lambda} \kappa_{\lambda} \left(4\pi I_{b\lambda} - G_{\lambda}\right) d\lambda \tag{17}$$

For each time step, Eq. (13) is solved for G_{λ} by using the temperature distribution. Since Eq. (13) represents spectral properties, the number of equations solved at each cell center is equivalent to the chosen wavelength intervals. Therefore, the cost of simulation is directly proportional to the number of spectral equations times the total number of cell centers. The net emission is then calculated using Eq. (17), while Eq. (16) is solved with $\nabla \cdot \mathbf{q}_{\text{rad}}$ inserted into it. The new temperature distribution obtained by solving Eq. (16) is again used by Eq. (13) to solve for new G_{λ}. This process is repeated until the relative difference between the temperature distributions, for the successive iterations, is below the prescribed tolerance (in the present work, 10^{-3}). An algorithm 1 is presented describing the coupling procedure. It should be noted that the coupling scheme converges at a linear rate.

III. Verification

The verification scheme is performed in two steps. The code verification is performed by comparing the numerical solution of RTE with the analytical one and is presented in Section III.A. Sections III.B-III.E present the solution verification cases where the temperature histories computed by pure conduction are compared with the ones computed by conduction coupled with radiative emission. Since Eqs. (15) and (16) refer to heat transfer through the same solid object, for a total heat flux at the heating surface, both methods should arrive at the same results. The total heat flux boundary condition can be a temperature profile or a heat flux profile along the surface.

The material used in the solution verification cases is LI-900. The thermal conductivities (both k_{eff} and k_{s+g}), absorption, and extinction coefficients for LI-900 are taken from Marschall et al. [27]. The values for specific heat capacity and density of LI-900 are taken from Williams et al. [30]. The domain of the wavelength-dependent optical (absorption and extinction) coefficients taken from Marschall et al. [27] is between 0.1 μm to 100 μm, and the same domain is taken as wavelength range with 101 intervals for the simulations. As seen from Eq. (10), the absorption coefficient plays an important role in radiative heat transfer. The value of the absorption coefficient between any two data points is calculated through interpolation. Therefore, the minimum value for the number of wavelength intervals is equal to the number of data points, which has been used in this work. The method of using the number of data points as the number of spectral equations (Eq. (13)) to be solved for internal radiation is termed as *Kappa Resolved Model* [31]. It was observed that the wavelength range and the number of intervals considered in this work denote the minimum values above which the simulated solution does not change. The simulations solve the energy equation only. Marshak boundary condition, as defined by Eq. (14), is applied at both front and back surfaces for all the solution verification cases. It should be noted that the simulated solutions presented for all the cases in this section are grid independent.

It should also be noted that the terms 'Absolute error,' 'Relative error,' 'RMS error,' and 'Relative max norm error'

Algorithm 1 Coupling scheme between heat conduction and radiation transfer equation

1: Input initial temperature (T_0), initial time (t_0), final time (t_f), time step size (Δt), wavelength range (λ_0, λ_f), number of wavelength intervals (n_λ), tolerance (tol), and boundary conditions
2: Read the mesh, initial and boundary values
3: Set time $t = t_0$, time step counter $n = 0$, and temperature $T = T_0$
4: Assign wavelengths $\lambda = \left[\lambda_0, \lambda_0 \left(\frac{\lambda_f}{\lambda_0}\right)^{\frac{1}{n_\lambda - 1}}, \ldots, \lambda_0 \left(\frac{\lambda_f}{\lambda_0}\right)^{\frac{n_\lambda - 2}{n_\lambda - 1}}, \lambda_f\right]$
5: Set $\nabla \cdot \mathbf{q}_{\text{rad}} = 0$, $T^1 = T_0$
6: **while** $t < t_f$ **do**
7: Increment time: $t = t + \Delta t$, $n = n + 1$
8: Set $i = 1$, $err = 1.0$
9: Solve Eq. (13) using T^i for all the wavelengths (λ)
10: Calculate $(\nabla \cdot \mathbf{q}_{\text{rad}})^i$ using Eq. (17) over the wavelength range
11: **if** $i \neq 1$ **then**
12: Calculate $err = \left\| \frac{(\nabla \cdot \mathbf{q}_{\text{rad}})^i - (\nabla \cdot \mathbf{q}_{\text{rad}})^{i-1}}{(\nabla \cdot \mathbf{q}_{\text{rad}})^{i-1}} \right\|_2$
13: **end if**
14: **if** $err > tol$ **then**
15: Insert $(\nabla \cdot \mathbf{q}_{\text{rad}})^i$ and solve Eq. (16) to get T^{i+1}
16: Assign i = i + 1
17: Goto Step 9
18: **end if**
19: Solve Eq. (16) with $(\nabla \cdot \mathbf{q}_{\text{rad}})^i$ inserted to get T^* for time t
20: Assign $T^1 = T^*$
21: **end while**

mentioned in the context of this work are defined as:

$$\text{Absolute error} = T_{\text{PC}} - T_{\text{RTE}} = \Delta T \tag{18}$$

$$\text{Relative error} = \frac{\Delta T}{T_{\text{PC}}} \tag{19}$$

$$\text{RMS error} = \left[\frac{\sum_{i=1}^{nt} \left(T_{\text{PC}_i} - T_{\text{RTE}_i}\right)^2}{nt}\right]^{1/2} \tag{20}$$

$$\text{Relative max norm error} = \frac{\|T_{\text{PC}} - T_{\text{RTE}}\|_\infty}{\|T_{\text{PC}}\|_\infty} \tag{21}$$

where 'PC' and 'RTE' denote pure conduction and conduction coupled with radiative emission methods, respectively, 'nt' represent the number of time steps, and $\|\cdot\|_\infty$ denote the infinity norm.

A. Comparison with an analytical solution

A simplified analytical solution is used to verify the numerical model of the RTE. This particular study's objective is to ensure the code's numerical correctness. To achieve that, all the parameters, except G_λ, are assumed to be constants, that is, $\kappa_\lambda = 1$ m^{-1}, $\beta_\lambda = 1/3$ m^{-1}, and $I_{b\lambda} = 1/(4\pi)$ W/m^2-μm-sr, in Eq. (13). A 1-D domain is considered, transforming Eq. (13) into an ordinary differential equation. The numerical and analytical solutions are presented in Fig. 1 as a function of non-dimensional variables. The numerical solution compares well with the analytical one, as seen in Fig. 1 with a L^2-norm error of 5.33×10^{-6}. These results only indicate that the code implements the RTE model faithfully and, therefore, does not provide any insight into the accuracy of the coupling scheme.

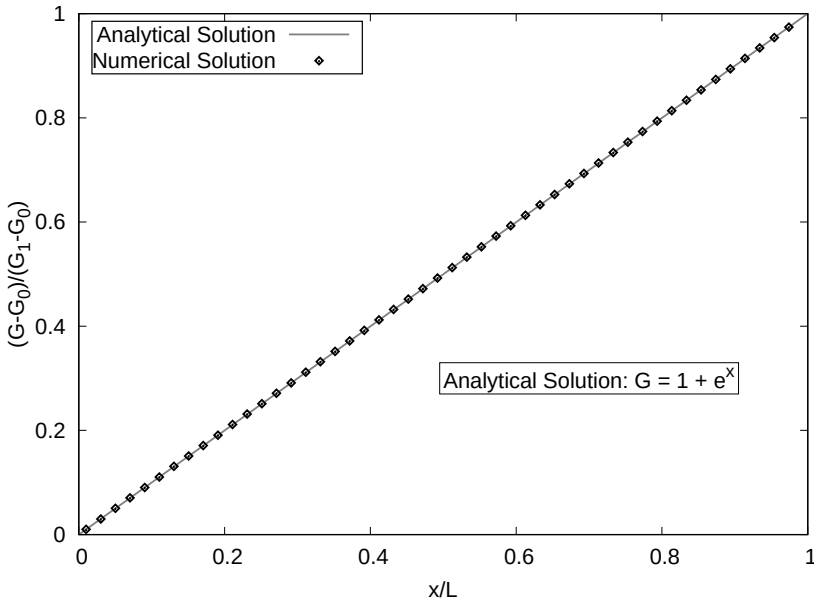

Fig. 1 Comparison of the numerical solution of an ordinary differential equation of RTE to its analytical counterpart

B. Marschall et al. Test Cases

Marschall et al. [27] test cases include three 1D cases: radiant heating, arc-jet heating, and space shuttle entry. Figure 2 illustrates the schematic of the test cases. In these test cases, the sample is heated by applying a temperature history at the heating surface. The wall of the sample, based on the test case, is either maintained at constant temperature or is assumed to be adiabatic and impermeable. A verification study is conducted by comparing the temperature histories computed using pure conduction with the ones computed using conduction coupled with radiative emission at different locations within the sample for each test case.

1. Radiant Heating

A 1.25 cm thick sample is heated for the radiant heating test. The pressure at the heating surface is 1 atm, and the temperature increases from 256 K to 1228 K in 15 seconds and remains constant for the remainder of the heating time. The temperature at the back face of the sample is kept at 256 K for the entire period.

The results from this simulation are illustrated in Fig. 3. Figure 3(a) shows the temperature histories at different thermocouple (TC) locations within the material for pure conduction and conduction coupled with radiative emission. The absolute and relative errors between the temperature histories calculated from both methods, the formulations of which are expressed in Eqs. (18) and (19), are shown in Fig. 3(b). It can be seen that the maximum absolute error is around 35 K, and the maximum relative error is less than 4% between the two methods. These maximum errors occur at around 15 seconds of heating time and due to high-temperature gradients. The high-temperature gradients are caused due to high heating times and occur within the shallow regions of the heating surface.

The RMS error and relative max norm error, which are calculated as expressed in Eqs. (20) and (21) for different TC locations, are presented in Table 1. The RMS error shows the average deviation of temperatures predicted by the coupling scheme when compared with the pure conduction one. Based on the values of RMS error, it can be deduced that most of the discrepancy between the two methods occurs due to high-temperature gradients, as seen in Fig. 3. On the other hand, the relative maximum norm error indicates the measure of the accuracy of the coupling scheme and based on the values, it can be concluded that the coupling scheme computes the temperatures accurately.

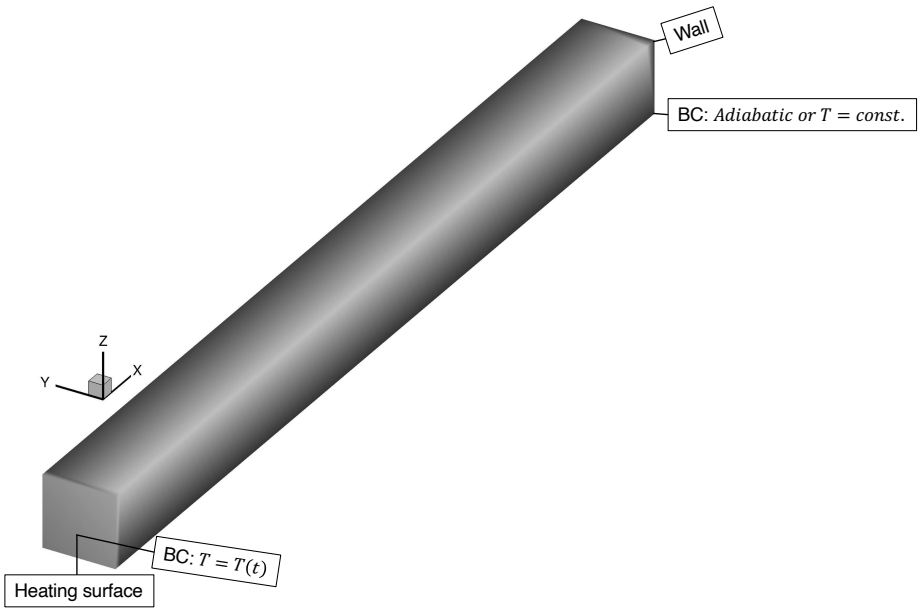

Fig. 2 Schematic of Marschall et al. test cases

Table 1 Error analysis between temperature histories at the thermocouple locations for radiant heating case

x, cm	RMS Error, K	Relative max norm error, %
0.10	14.70	3.07
0.30	15.90	2.48
0.50	9.49	1.41

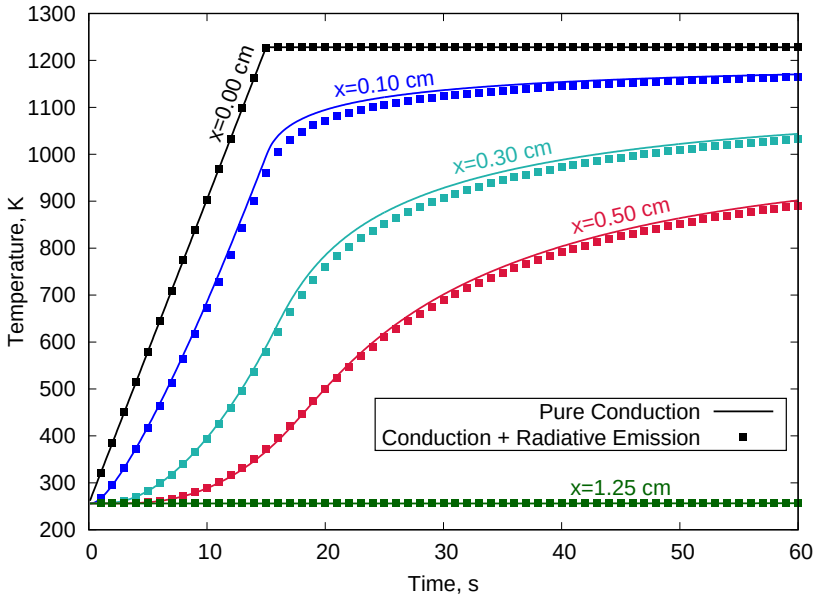

(a) Temperature histories at various locations within the sample

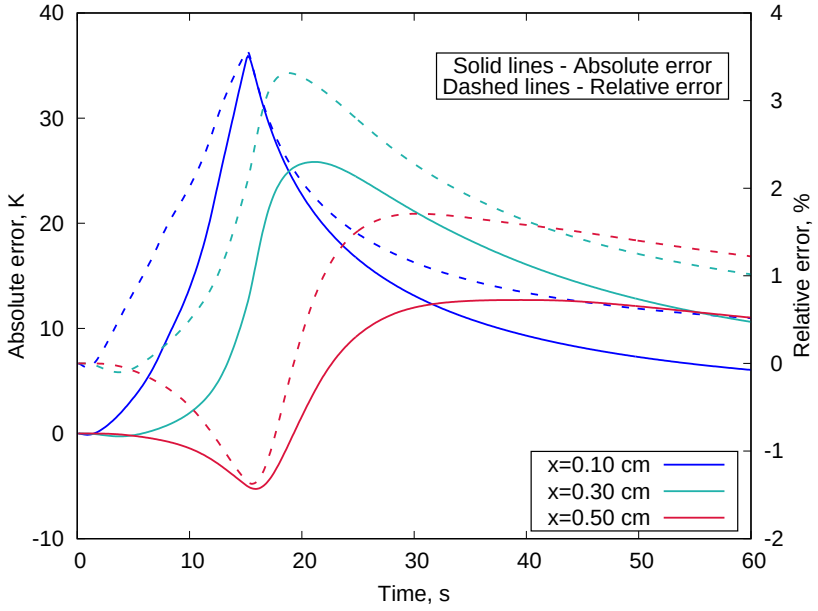

(b) Absolute and relative errors between the temperatures of two methods

Fig. 3 Comparison between pure conduction and conduction coupled with radiative emission for radiant heating case

2. Arc-jet Heating

The second case is the arc-jet heating test on a 4 cm sample. While the sample's back surface is impermeable and adiabatic, the front surface is at a pressure of 0.01 atm and is heated, increasing the temperature from 300 K to 1700 K in 5 seconds, remaining at 1700 K for another 3 minutes, and then following a cooling curve.

The results from the simulation of the arc-jet heating case are given in Fig. 4. Figure 4(a) shows the temperature histories for both pure conduction and conduction coupled with radiative emission at TC points within the sample. The absolute and relative difference between the temperature histories calculated from both the methods are shown in Fig. 4(b). The differences show that the maximum absolute error between the two methods is below 100 K whereas the maximum relative error is below 17%. These maximum differences in temperatures between the two methods occur due to high-temperature gradients. Apart from the maximum values, it can be seen that the discrepancy between the temperatures, especially for 0.50 cm and 1.00 cm locations, exists during rapid heating (the first 5 seconds), the period after the rapid heating (between 5 seconds and 185 seconds), and also during the abrupt cooling period (between 185 seconds and 200 seconds). The TC locations – 0.50 cm and 1.00 cm – attain high temperatures during a part of the heating time, which cause the above-mentioned discrepancies.

The RMS error and relative max norm error for various TC locations within the sample are presented in Table 2. It can be observed that the average deviation of the temperatures predicted by the coupling scheme from the pure conduction ones decreases along the sample length. The high values of deviations occur for TC points 0.50 cm and 1.00 cm due to large temperature gradients and high temperatures. The relative max norm error seems to indicate that the coupling scheme accurately predicts the temperatures.

Table 2 Error analysis between temperature histories at the thermocouple locations for arc-jet heating case

x, cm	RMS Error, K	Relative max norm error, %
0.50	26.85	5.98
1.00	16.87	3.12
2.00	8.63	2.32
3.00	5.77	1.72
4.00	2.73	0.95

3. Space Shuttle Entry

The third case is the space shuttle entry test on a 5 cm sample. The front surface kept at 300 K and 0.1 atm is heated to 1200 K over 350 seconds, remaining at 1200 K for another 11 minutes. The front surface later undergoes a varying temperature curve as shown in Fig. 5(a). The back surface of the sample is set to be adiabatic and impermeable. The results from the simulation of the space shuttle entry case are shown in Fig. 5. Figure 5(a) shows the temperature histories at different thermocouple points within the sample for both pure conduction and conduction coupled with radiative emission. Figure 5(b) illustrates the absolute error and relative error between the temperature histories calculated from both methods. It can be noted that the maximum absolute error and maximum relative error between the two methods are below 8 K and 1.2%, respectively. The low-temperature gradients due to slower heating time cause the difference in the temperatures between the methods to be minimal.

It can also be seen that the average deviations measured through RMS error and relative maximum norm errors of temperatures predicted by the coupling scheme are very low due to small temperature gradients. The values for RMS error and relative max norm error for different TC points are listed in Table 3.

It should be noted that the solutions as shown in Figs. 3, 4, and 5 show excellent agreement between temperatures predicted by pure conduction and conduction coupled with radiative emission methods. The differences between the temperature histories of both methods are due to high-temperature gradients. It was also observed that high temperatures in the arc-jet heating case (III.B.2) also cause differences in the results. The radiative part of the *effective* thermal conductivity is computed by applying Rosseland approximation [24–26] to the fiber-to-fiber re-radiation problem. The approximation assumes that the medium is optically thick and isotropic. At high-temperature gradients, the medium is

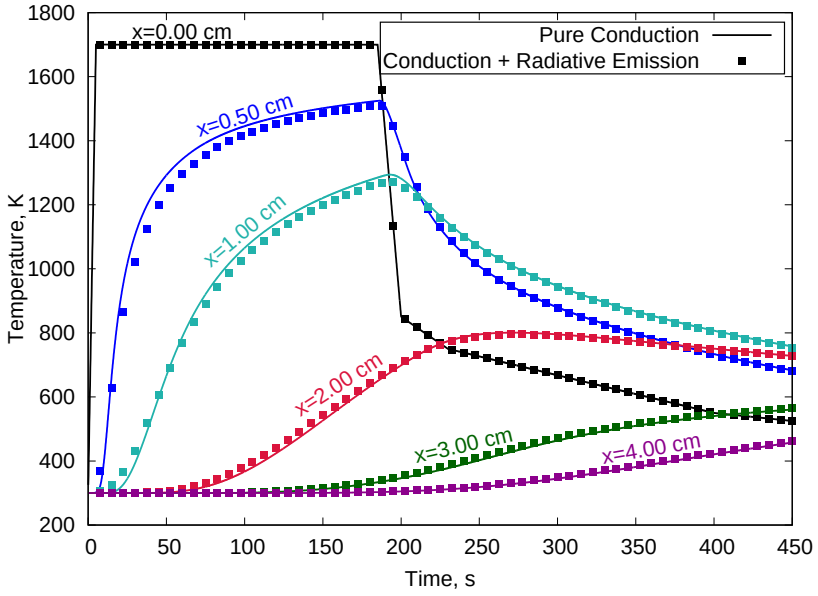

(a) Temperature histories at various locations within the sample

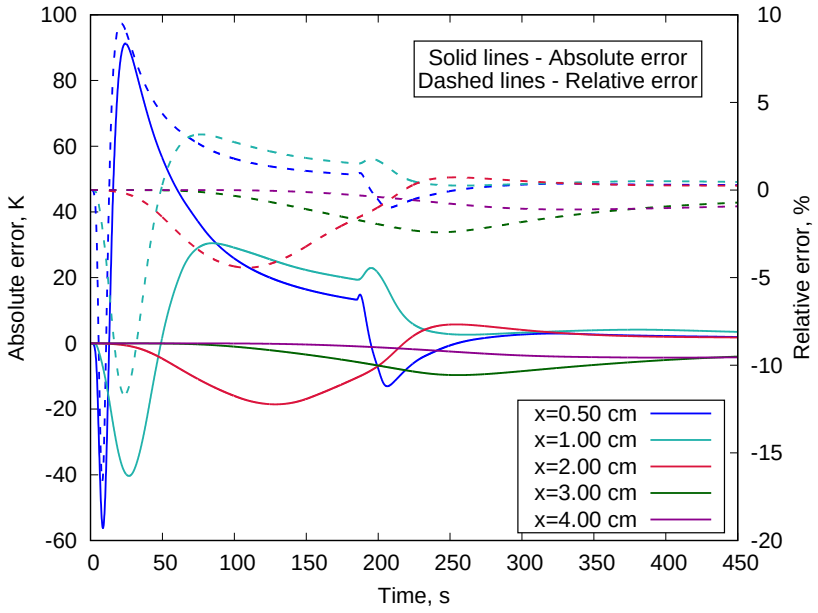

(b) Absolute and relative errors between the temperatures of two methods

Fig. 4 Comparison between pure conduction and conduction coupled with radiative emission for arc-jet heating case

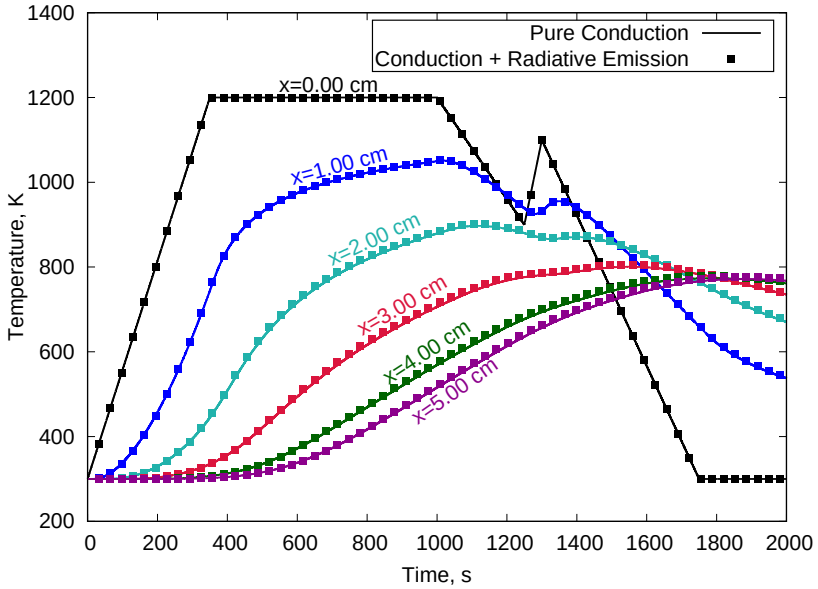

(a) Temperature histories at various locations within the sample

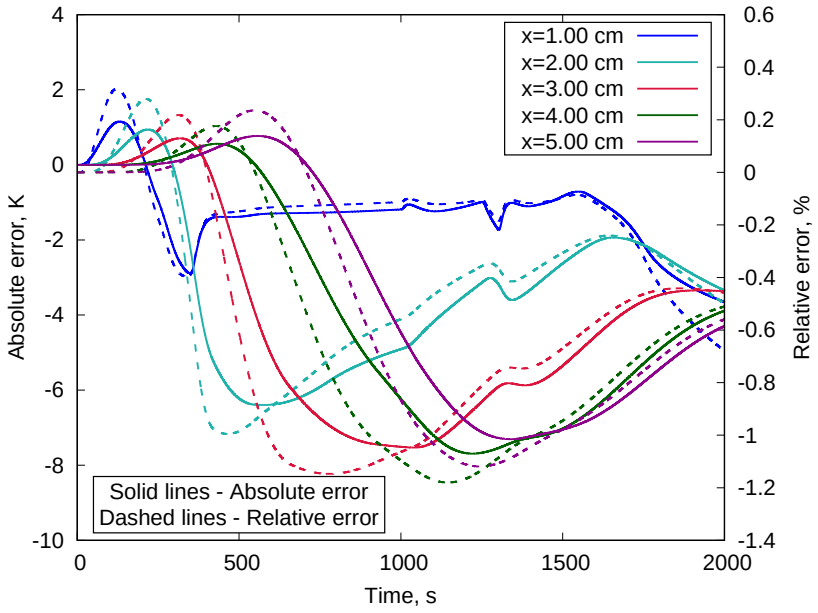

(b) Absolute and relative errors between the temperatures of two methods

Fig. 5 Comparison between pure conduction and conduction coupled with radiative emission for space shuttle entry case

Table 3 Error analysis between temperature histories at the thermocouple locations for space shuttle entry case

x, cm	RMS Error, K	Relative max norm error, %
1.00	1.63	0.35
2.00	3.92	0.71
3.00	4.98	0.94
4.00	4.90	0.99
5.00	4.53	0.95

not isotropic in nature, which makes the approximations invalid [27, 28]. Therefore, the k_{eff} does not provide accurate values at large temperature gradients. Thus, the differences in the temperature histories for huge temperature gradients are due to inaccurate predictions from the pure conduction scheme. The other source of discrepancy between the results from both methods is high temperatures. The values of k_{s+g} for LI-900 were derived numerically through calibration by Marschall et al. [27]. At a specific temperature and pressure, $\nabla \cdot \mathbf{q}_{\text{rad}}$ is calculated, and k_{s+g} is determined by comparing radiation source term with pure conduction values. However, it was found that the uncertainty of these calibrated values increased with an increase in temperature. Therefore, the coupling scheme computes inaccurately at high temperatures due to erroneously calibrated k_{s+g} values that lead to differences between the results.

To avoid inaccurate predictions of temperatures at large temperature gradients, the conduction coupled with radiative emission scheme is suggested over the pure conduction scheme. However, to prevent discrepancies in the results at high temperatures, the time-dependent temperature profiles, to be given as a boundary condition to the heating surface, for all the verification cases presented hereafter will be constrained to be below or around 1200 K.

C. 3D Block

The verification is performed on a Block mesh with dimensions of 1.25 cm, 0.625 cm, and 0.2 cm in x-, y-, and z-direction, respectively. The schematic of the 3D block test case is presented in Fig. 6. The boundary conditions for the radiant heating case, as given in Section III.B.1, are used to simulate the thermal response of the 3D Block. The temperature history at the heating surface and the constant temperature condition at the wall are illustrated in Fig. 6. Also, the mesh of the 3D Block, along with the TC locations, is presented in Fig. 6. The coordinates of TC locations are given in Table 4.

Table 4 Virtual thermocouple locations for 3D Block sample

TC#	Coordinates, m
1	(0.00000, 0.0030, 0.00150)
2	(0.00100, 0.0030, 0.00150)
3	(0.00300, 0.0030, 0.00150)
4	(0.00500, 0.0030, 0.00150)
5	(0.01250, 0.0030, 0.00150)

Figures 7(a) and (b) show the temperature contours for pure conduction as well as conduction coupled with radiative emission at the end of the heating period, respectively. It can be seen that the temperature contours for both methods are virtually identical, with an absolute error between the two methods at the end of the heating period being below 14 K, as shown in Fig. 7(c). The radiation source term contour at the end of the heating period is presented in Fig. 7(d). It can be seen that the radiation source term increases along the sample length and is maximum at the location where the relatively cold surface is receiving the heat. The animation of the complete simulation is provided in the Supplementary Material.

It can be noticed from Fig. 7(d) that the magnitude of the radiation source term increases from a negative to a

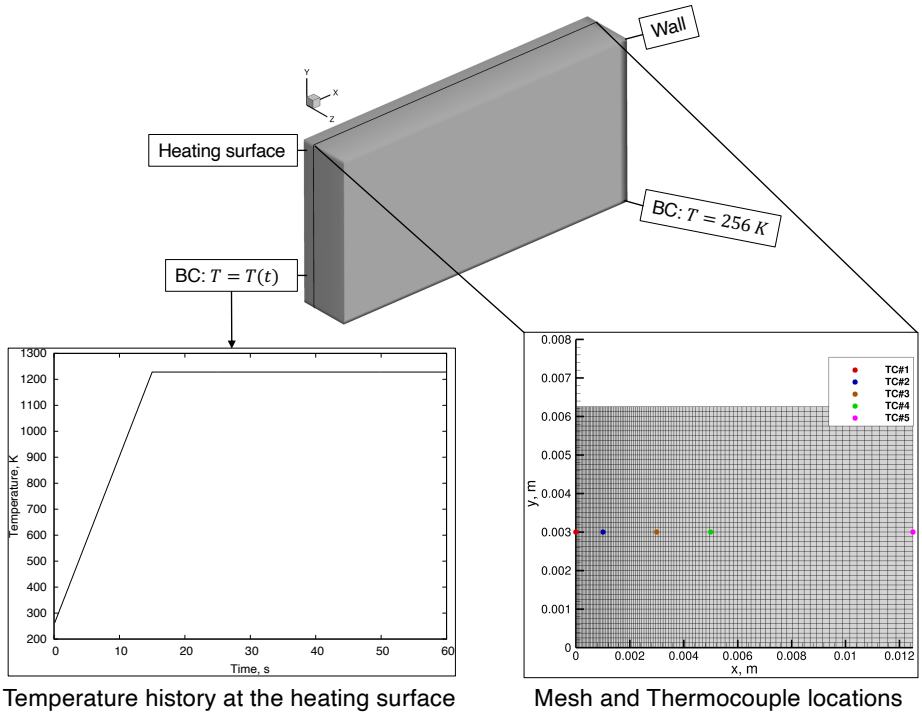

Fig. 6 Schematic of 3D Block test case

positive value in the direction of heat transfer. The radiation source term depicts a balance between the absorption and emission of heat energy. The regions near the heating surface reach a steady-state temperature. The material emits heat at these places, so the radiation source term is negative in value. On the other hand, the material absorbs heat at places where heat transfer occurs, indicating a positive value for the radiation source term. This behavior is observed for all the verification cases presented in this work.

To understand the thermal-response behavior in more detail, the temperatures predicted by both methods and their difference (both absolute and relative) at the TC locations are plotted as a function of heating time and are presented in Fig. 8. It can be observed that the temperature histories match well with the maximum absolute error below 40 K and maximum relative error below 4% between the two methods, respectively. These maximum errors occur due to high-temperature gradients. These histories and errors are also similar to those for the 1D case shown in Figure 3.

The RMS error and relative max norm error for various TC locations within the sample are presented in Table 5. The average deviation results in the form of RMS error are higher when compared to ones in Section III.B.1 which indicate that the results of the high-temperature gradient have more discrepancy for a 3D sample when compared to a 1D one. However, the relative max norm error shows the accuracy of temperatures predicted by the coupling scheme when compared with pure conduction ones.

Table 5 Error analysis between temperature histories at the thermocouple locations for 3D Block sample

TC#	RMS Error, K	Relative max norm error, %
2	16.40	3.30
3	18.04	2.75
4	11.35	1.68

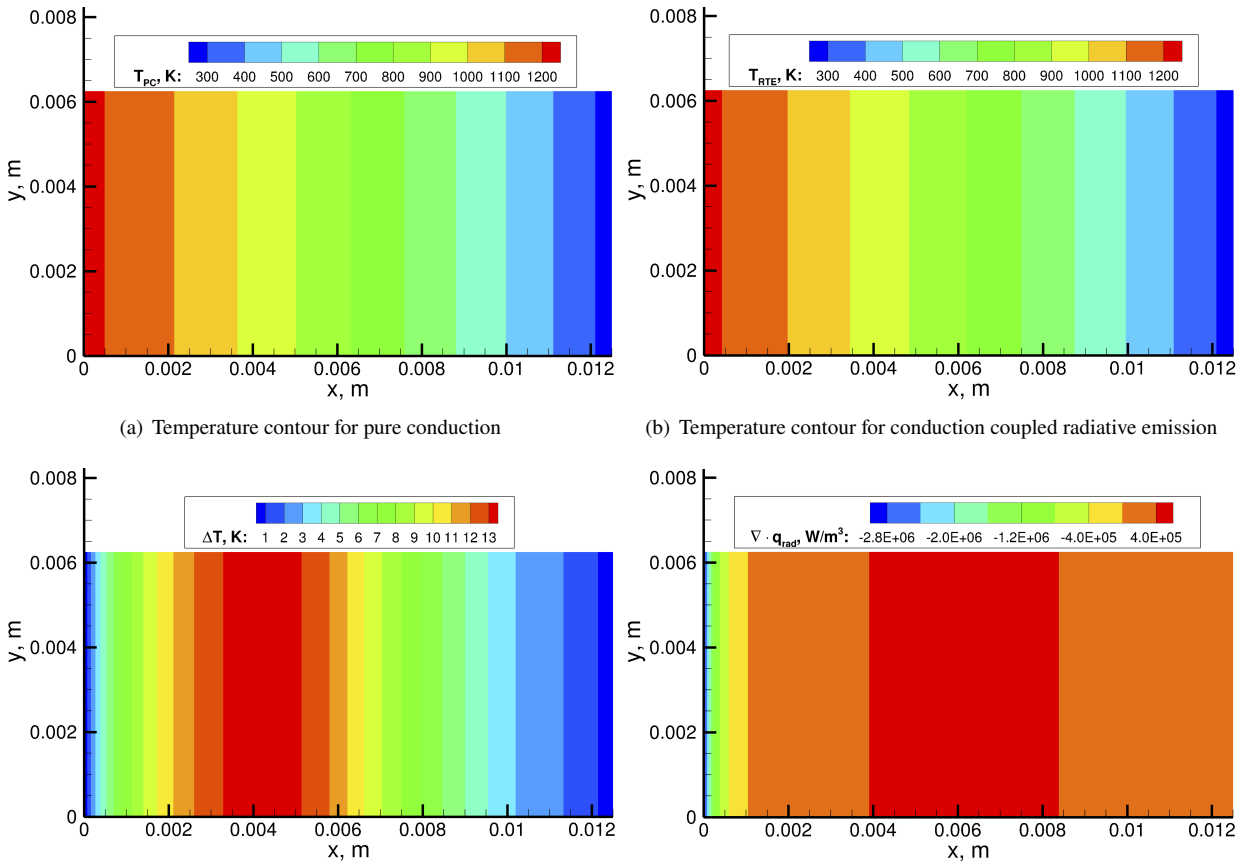

(a) Temperature contour for pure conduction

(b) Temperature contour for conduction coupled radiative emission

(c) Absolute error between temperatures

(d) Radiation source term

Fig. 7 Temperature and radiation source term contours for pure conduction and conduction coupled radiative emission for 3D Block case at the end of heating time

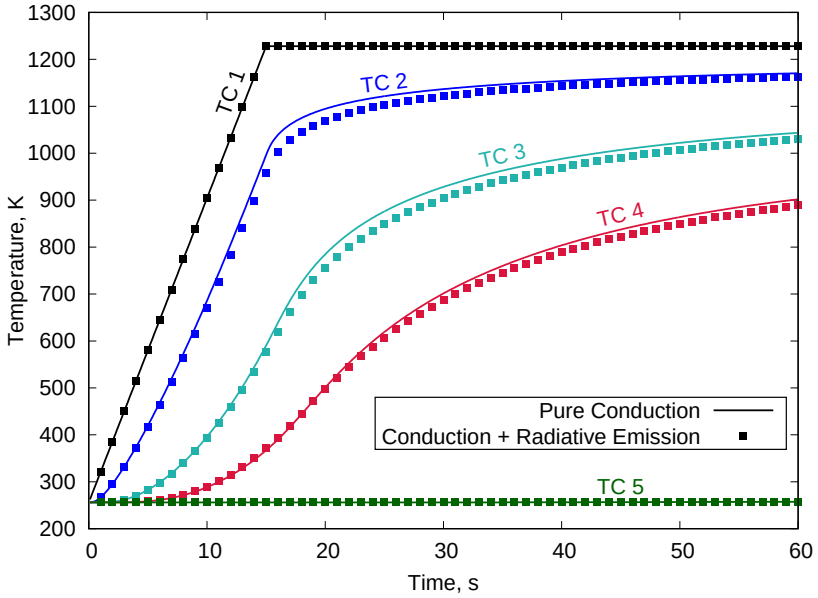

(a) Temperature histories at various locations within the sample

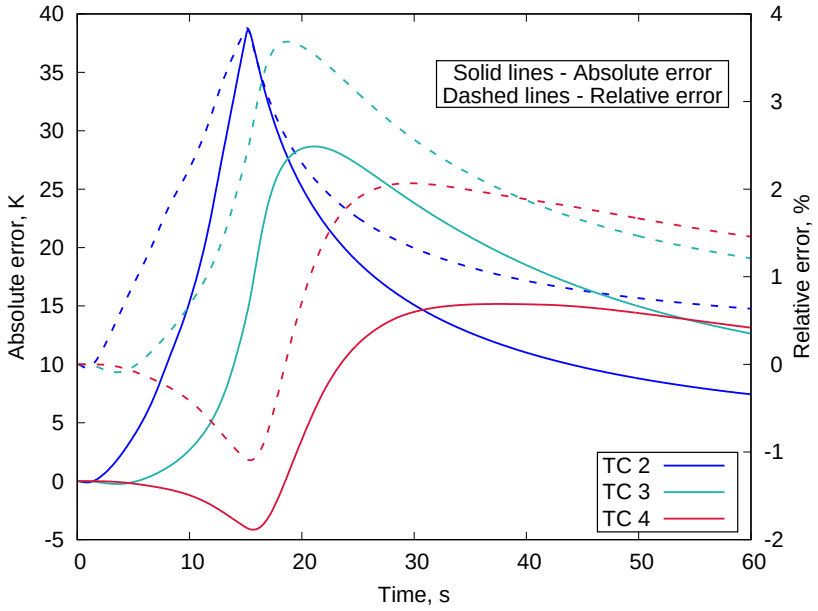

(b) Absolute and relative errors between the temperatures of two methods

Fig. 8 Comparison between pure conduction and conduction coupled with radiative emission for 3D Block case

D. IsoQ Sample

A 2D IsoQ sample is considered for performing the verification. The IsoQ sample test case schematic is presented in Fig. 9. The heating surface of the sample is heated from 300 K and 1 atm to time-dependent temperature profiles in 5 seconds and remains constant for the rest of the heating time. The wall of the sample is assumed to be adiabatic and impermeable. The temperature profiles imposed on the heating surface as a function of heating time are shown in Fig. 9. The TC locations and mesh of the sample are also presented in Fig. 9. The virtual TC locations for the IsoQ sample were taken from Weng et al. [19] for the verification study. The coordinates of TCs are listed in Table 6.

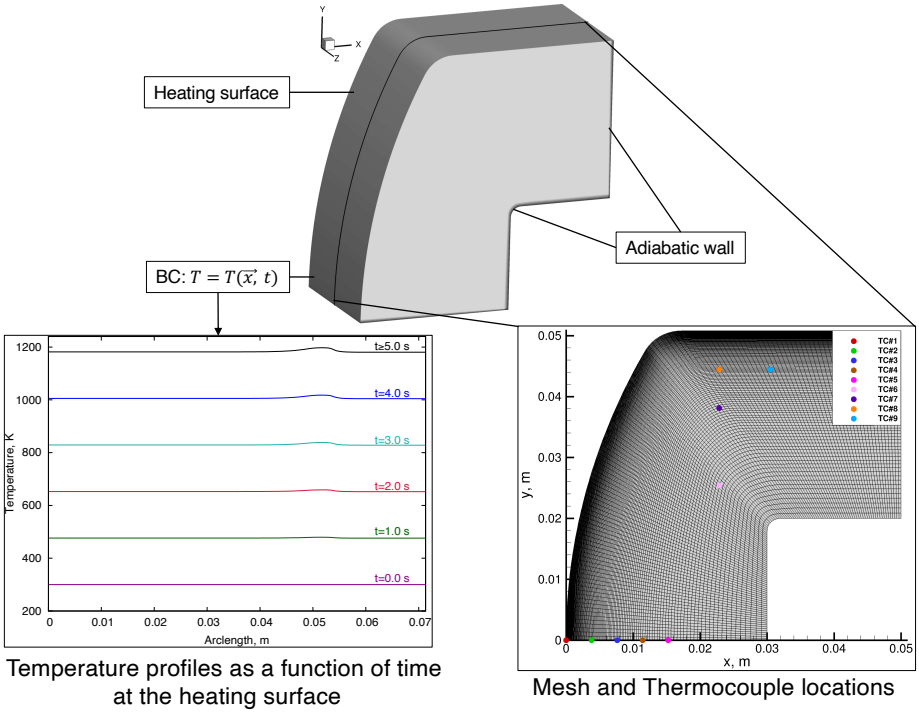

Fig. 9 Schematic of 2D IsoQ test case

The temperature contours, a contour of the temperature difference between the methods, and a radiation source term contour at the end of the heating period are shown in Fig. 10 for the IsoQ sample. The temperature contours are visibly similar for the two methods. The absolute error between the temperature contours shows a maximum value of around 45 K that occurs at the shoulder region, as seen in Fig. 10(c), and is due to the high-temperature gradients at that location. The radiation source term is in the form of a patch across the region where the relatively colder surface is receiving the heat, as can be seen in Fig. 10(d). The animation of the complete simulation is provided in the Supplementary Material.

To quantify the difference of temperatures between the methods, the temperature histories at different TC locations, and absolute and relative error in the temperatures between the two methods are illustrated in Fig. 11. The TC locations are given in Table 6. Figures 11(a) and (b) represent the temperature histories for TCs along the stagnation line and in-depth ones, respectively. The absolute and relative error in temperatures between the two methods are presented in Fig. 11(c). The temperature histories for both methods match well, with the maximum absolute and relative error between the methods being around 20 K and 3%, respectively. These maximum values are attributed to high-temperature gradients caused during the heating period.

The low magnitude of RMS errors and relative max norm errors for different TC locations, as shown in Table 7, indicate the accuracy of the coupling scheme in computing temperatures for a 2D sample.

Table 6 Virtual thermocouple locations for IsoQ sample

TC#	Coordinates, m
1	(0.00000, 0.00000, 0.0)
2	(0.00381, 0.00000, 0.0)
3	(0.00762, 0.00000, 0.0)
4	(0.01143, 0.00000, 0.0)
5	(0.01542, 0.00000, 0.0)
6	(0.02286, 0.02540, 0.0)
7	(0.02286, 0.03810, 0.0)
8	(0.02286, 0.04445, 0.0)
9	(0.03048, 0.04445, 0.0)

Table 7 Error analysis between temperature histories at the thermocouple locations for 2D IsoQ sample

TC#	RMS Error, K	Relative max norm error, %
2	9.95	2.63
3	4.90	2.17
4	1.32	1.02
5	0.22	0.18
6	0.02	0.02
7	0.49	0.41
8	2.56	1.39
9	3.02	1.29

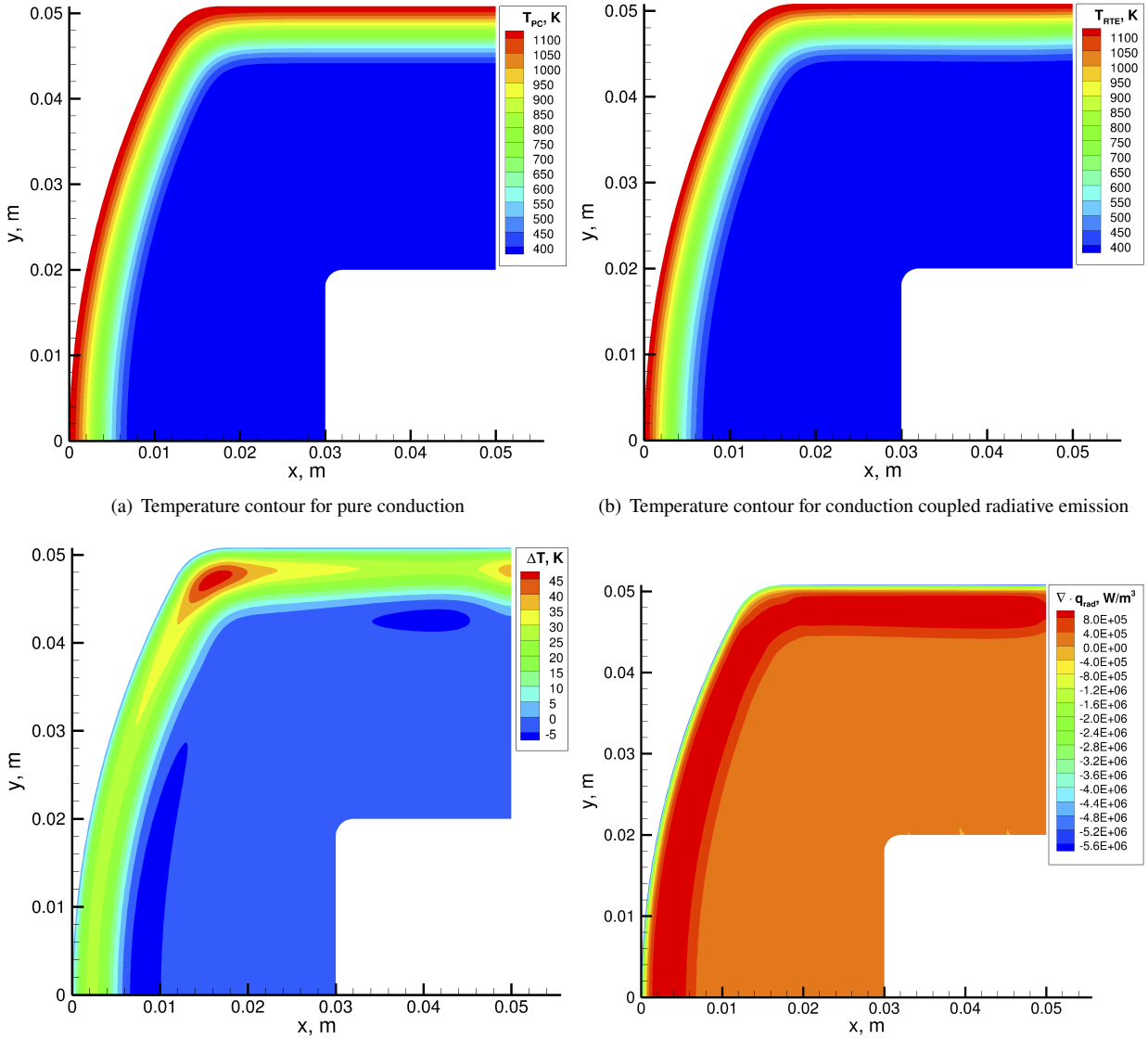

(a) Temperature contour for pure conduction

(b) Temperature contour for conduction coupled radiative emission

(c) Absolute error between temperatures

(d) Radiation source term

Fig. 10 Temperature and radiation source term contours for pure conduction and conduction coupled radiative emission for IsoQ sample at the end of heating time

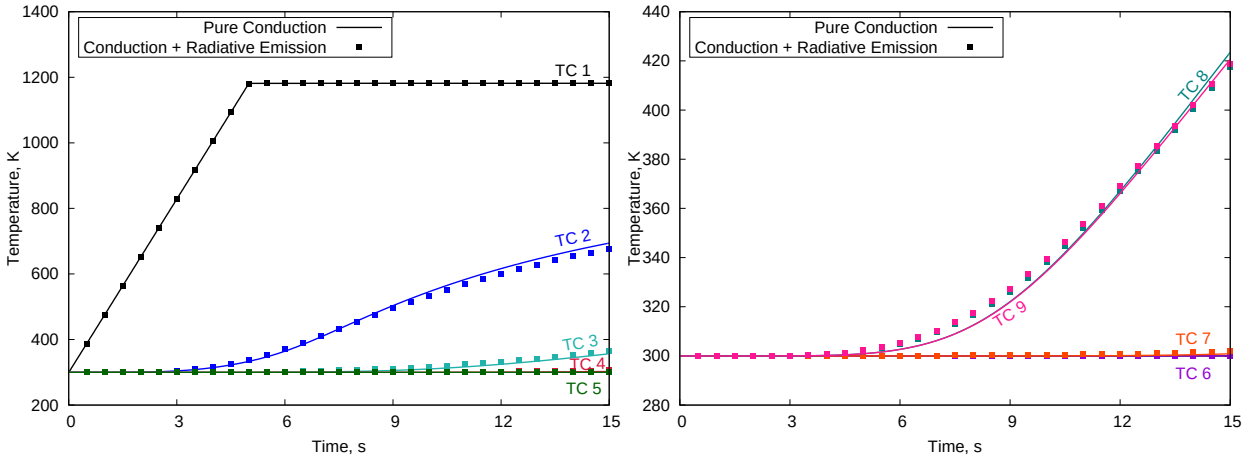

(a) Temperature histories at various locations within the sample (TC# 1–5)

(b) Temperature histories at various locations within the sample (TC# 6–9)

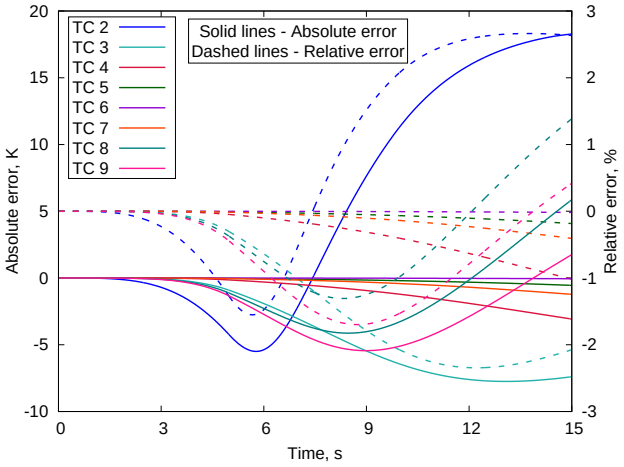

(c) Absolute and relative errors of temperature between two methods

Fig. 11 Comparison between pure conduction and conduction coupled with radiative emission for IsoQ sample

E. Stardust Return Capsule

The coupling scheme is applied to the Stardust sample return capsule (SRC) heat shield. The schematic used for the verification case is presented in Fig. 12. A temperature profile as a function of heating time is given as the boundary condition at the heating surface. The heating starts at 298 K and 0.01 atm, and the temperature profile at the front surface increases linearly until 8 seconds and remains constant thereafter, as shown in Fig. 12. The temperature profile is the modified version of a steady profile that the Stardust capsule achieves when exposed to heat flux corresponding to t = 34 s of its travel [32]. The back surface is set to be adiabatic and impermeable. A modified version of Stardust mesh for the simulation is reconsidered [20], which is illustrated in Fig. 12 along with the TC locations. The virtual TC locations correspond to the ones used by Weng et al. [20]. The coordinates of TCs are given in Table 8.

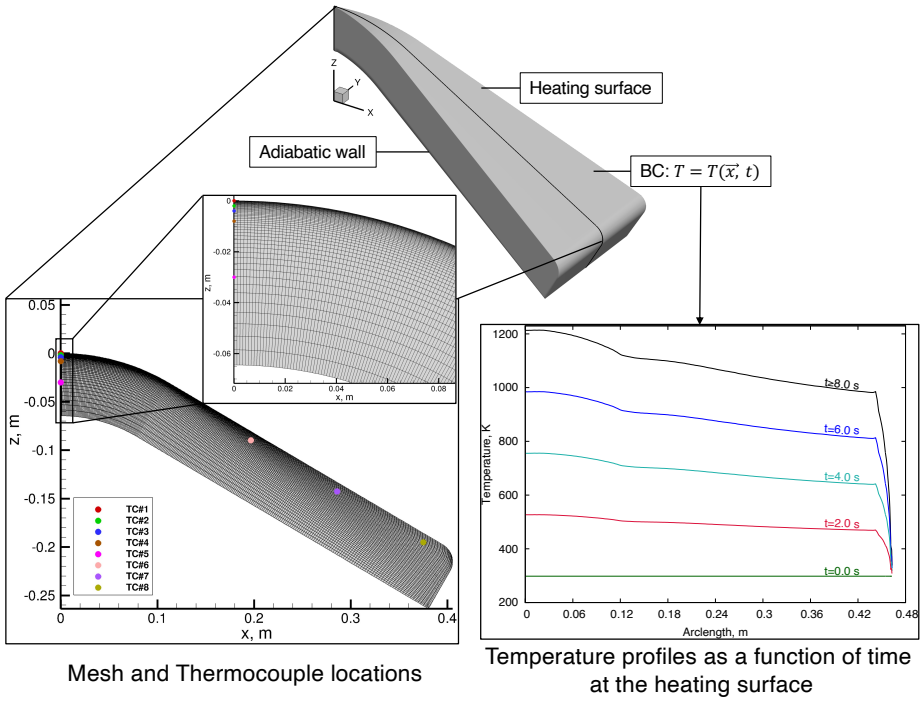

Fig. 12 Schematic representation of Stardust heat shield

The temperature contours, a contour illustrating the difference in temperatures of both methods, and a radiation source term contour at the end of the heating period are presented in Fig. 13. The temperature contours, as seen in Figs. 13(a) and (b), appear similar for both methods. The absolute error between the temperatures of both methods is noted to be high along the shoulder due to the large temperature gradients with the maximum value around 72 K as shown in Fig. 13(c). Similarly, Fig. 13(d) shows the contour of the radiation source term, which is higher near the shoulder location. The animation of the complete simulation is provided in the Supplementary Material.

The temperature histories of both methods and their differences are plotted to quantify the accuracy of the coupling scheme. Figure 14 illustrates the temperature histories and differences in temperatures between the methods as a function of heating time for various TC locations. The TC location coordinates are given in Table 8. The temperature histories for TCs along the stagnation line and the shoulder are presented in Figs. 14(a) and (b), respectively. The temperature histories of the two methods match satisfactorily. The absolute and relative errors between the temperatures of the two methods are presented in Fig. 14(c). It can be seen that the maximum absolute and relative error between the temperatures at different TCs are around 70 K and below 10%, respectively. These maximum values are caused due to high-temperature gradients that affect the temperature predictions using the pure conduction scheme within the shallow regions of the heating surface.

Table 8 Virtual thermocouple locations for Stardust entry capsule

TC#	Coordinates, m
1	(0.0000, 0.0, 0.0000)
2	(0.0000, 0.0, −0.0020)
3	(0.0000, 0.0, −0.0040)
4	(0.0000, 0.0, −0.0080)
5	(0.0000, 0.0, −0.0300)
6	(0.1969, 0.0, −0.0899)
7	(0.2861, 0.0, −0.1425)
8	(0.3753, 0.0, −0.1950)

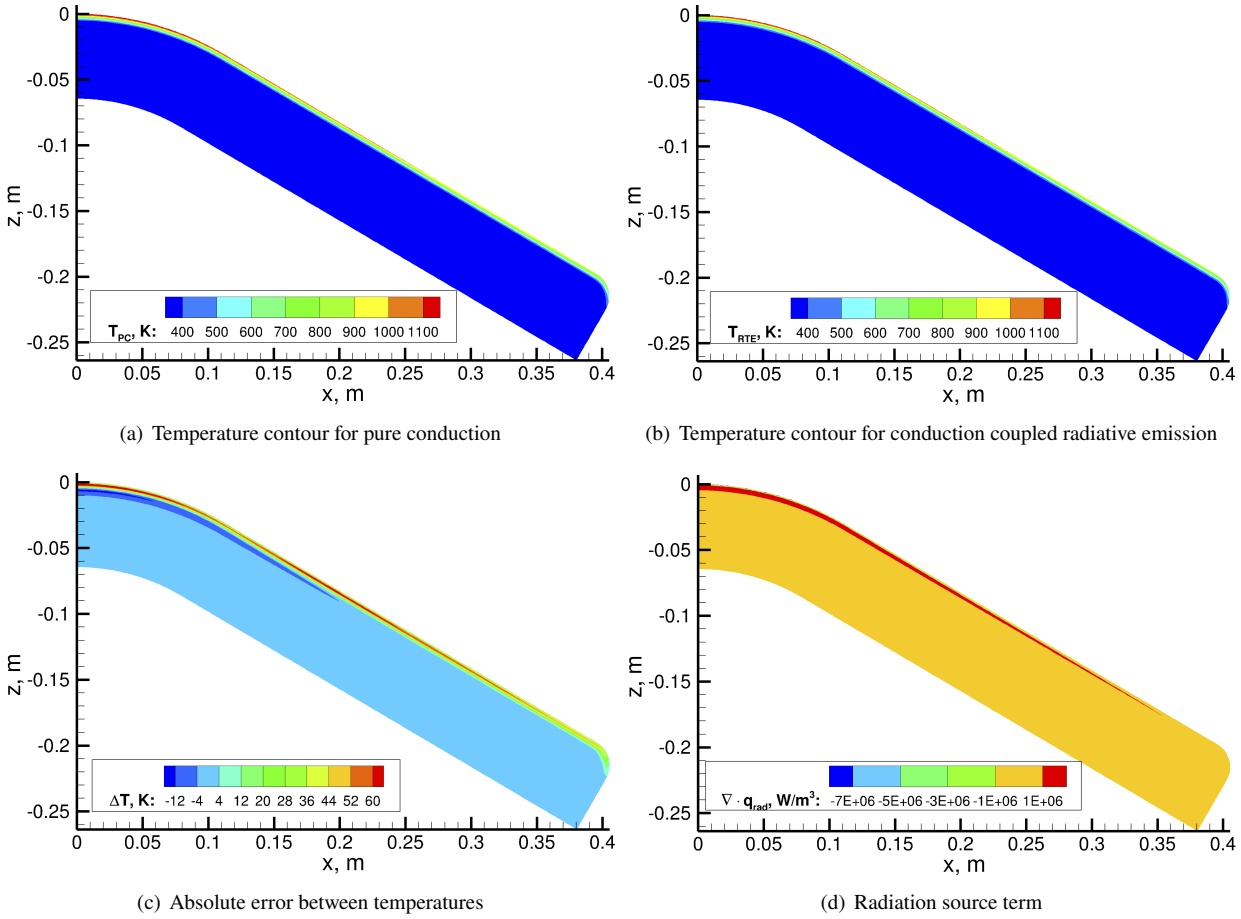

(a) Temperature contour for pure conduction

(b) Temperature contour for conduction coupled radiative emission

(c) Absolute error between temperatures

(d) Radiation source term

Fig. 13 Temperature and radiation source term contours for pure conduction and conduction coupled radiative emission for Stardust entry capsule at the end of heating time

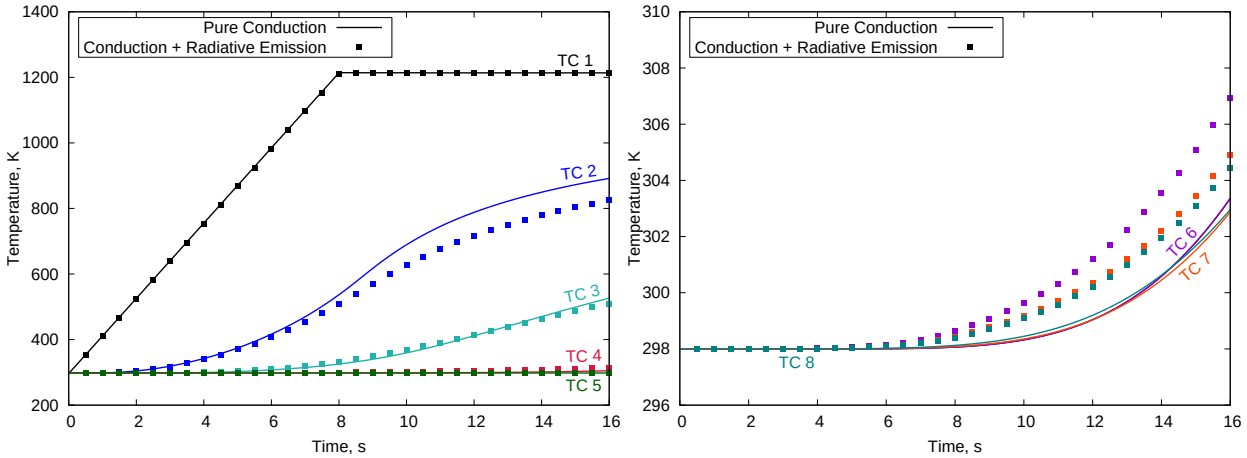

(a) Temperature histories at various locations within the sample (TC# 1–5)

(b) Temperature histories at various locations within the sample (TC# 6–8)

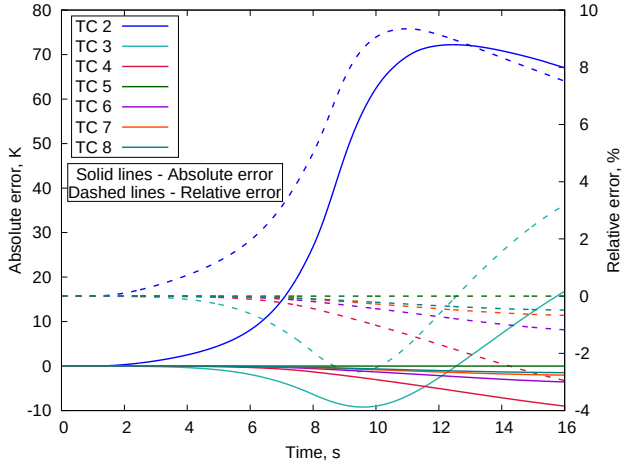

(c) Absolute and relative errors of temperature between two methods

Fig. 14 Comparison between pure conduction and conduction coupled with radiative emission for Stardust entry capsule

The RMS error and relative max norm error at different TC points are presented in Table 9. The RMS error at TC#2 is very high when compared to other thermocouple locations due to the effect of large temperature gradients. The relative max norm error for various TC points is satisfactory, indicating the accuracy of the coupling scheme in predicting the temperatures when compared with the pure conduction scheme.

Table 9 Error analysis between temperature histories at the thermocouple locations for Stardust entry capsule

TC#	RMS Error, K	Relative Max norm, %
2	46.40	8.10
3	6.16	3.19
4	3.96	2.95
5	0.00	0.00
6	1.64	1.18
7	0.98	0.67
8	0.73	0.49

It can be seen from the verification study that temperature profiles as a function of heating time were given as boundary conditions at the heating surface. When a heat flux is provided as a boundary condition, the heating surface temperatures are extrapolated from the heat conduction equation. Since the two methods use different thermal conductivity's $\left(k_{\text{eff}} \text{ and } k_{s+g}\right)$, the extrapolated temperatures are distinct. Since Eqs. (15) and (16) are boundary-value problems, different temperatures at the boundary would result in different solutions.

As stated before, it was observed that at higher temperatures, the coupling scheme furnishes inaccurate values of temperatures due to uncertainty in calibrated k_{s+g} values. In order to run the simulations at higher temperature profiles, it would be necessary to re-calibrate k_{s+g} values to refrain from extrapolation.

IV. Laser Ablation

In this section, the material response to the laser heating is simulated using both pure conduction and conduction coupled with radiation emission schemes. Unlike Section III, the temperature histories predicted by the two methods would differ due to a spectral heat flux boundary condition. Simulations are performed to study the thermal response behavior when the material is irradiated by the lasers used in White [7] experiments. Additionally, the role of the absorption coefficient of the material is investigated by comparing the thermal-response behaviors of the material when irradiated by various types of lasers and modified optical properties. The simulations solve both energy and mass decomposition equations.

A. Material-response due to laser heating

Laser heating simulations are performed by mimicking the experiments conducted by White [7] to understand the spectral contribution of the radiative heat flux. White [7] used Fiber and CO_2 lasers of wavelengths 1.07 μm and 10.6 μm, respectively, for heating various charring fibrous materials. The samples were exposed to lasers for 30 seconds at a constant heat flux of 115 W/cm^2. It should be noted that the simulation focuses on only the material response part of the experiment. Also, the experiments were conducted on carbon fiber felt, silica fiber felt, and glass-fiber-based materials. Due to the unavailability of thermophysical and optical properties for the materials used in the experiments, an amalgamated material is used for the simulation. The thermophysical properties of TACOT, a fictitious material replicating the properties of PICA [33], are used for the simulations. On the other hand, the optical properties of the LI-900 are assumed for the material. Therefore, the material in total is a combination of two different materials. It should be noted that though this amalgamated material does not exist, it is expected that the behavior observed would follow a general trend. Since only the material response part is focused and none of the experimental sample material properties are used for the simulations, no comparisons of numerical predictions with the experimental ones were made.

A sample of 2 cm long is considered. A schematic of the laser heating test case is presented in Fig. 15. The sample at 300 K starts heating up due to the laser heat flux imposed on the front surface. Three simulations were run: one

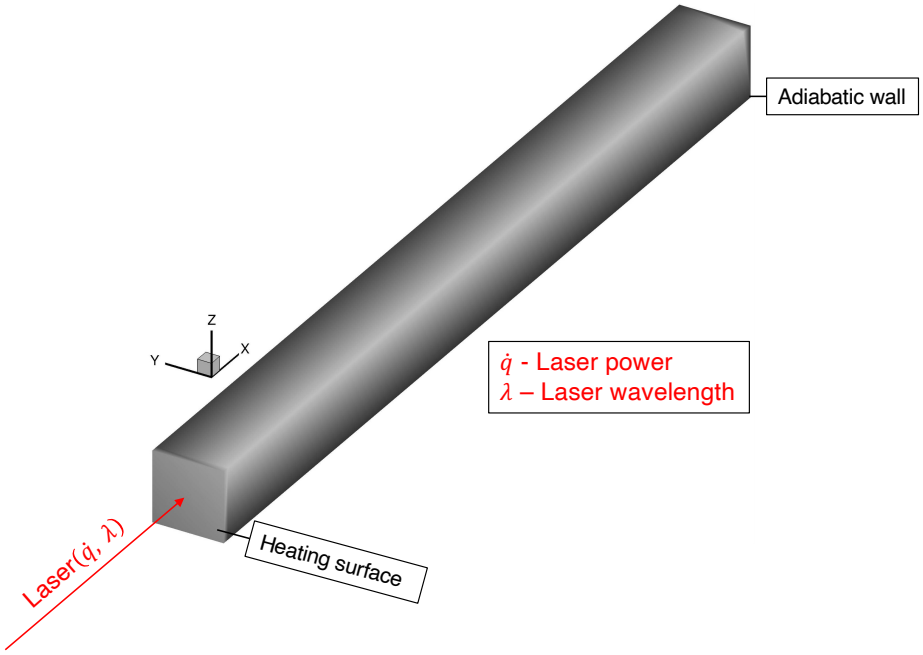

Fig. 15 Schematic of Laser heating test case

with pure conduction and the other two with conduction coupled with radiative emission for the two laser wavelengths. Since the available thermal conductivity table for TACOT was that of k_{eff}, the coupling scheme was performed by accounting for the conduction with k_{eff} and radiation with RTE but by assuming the Planck function to be zero. As stated before, the simulations solve both mass and energy equations for density decomposition and heat transfer through solid, respectively. A Neumann boundary condition at the heating surface and a Marshak boundary condition at the wall is applied to the RTE. A wavelength range from 0.1 μm to 100 μm and 101 wavelength intervals are chosen for the conduction coupled with radiative emission simulations.

The temperature and solid density histories as a function of heating time are presented in Fig. 16. The absorption and extinction coefficients $(\kappa_\lambda, \beta_\lambda)$ of the material for CO_2 laser wavelength and Fiber laser wavelength are given in Table 10. It should be noted that the material has higher absorption and extinction coefficients for CO_2 laser wavelength when compared to the Fiber laser wavelength. The higher magnitudes of these coefficients imply that the energy is absorbed within a thin layer of the material. On the other hand, the lower values of these coefficients indicate that the energy is deposited deep inside the sample leading to a different heat transfer response. In Fig. 16(a), it can be seen that the temperature histories for pure conduction and CO_2 laser is higher at the surface when compared to Fiber laser. The internal temperature histories for pure conduction and CO_2 laser also follow the same trend. However, the temperature histories within the material irradiated by the Fiber laser are higher compared to the other two cases. Since the internal temperatures are higher for the Fiber laser case, the rate of decomposition of the solid is also higher when compared to the other two methods, as can be seen in Fig. 16(b).

Figure 17 shows the temperature and solid density distribution along the sample length at the end of the heating period. It can be observed that the internal temperature distribution for the Fiber laser is higher when compared to the other two cases. Similarly, due to comparatively higher temperature distribution, the decomposition of the solid is higher within the material for the Fiber laser case, as illustrated in Fig. 17(b). The animation comparing all three simulations is provided in the Supplementary Material.

The extent to which the energy is deposited in the sample irradiated by two lasers is shown in Fig. 18. The energy

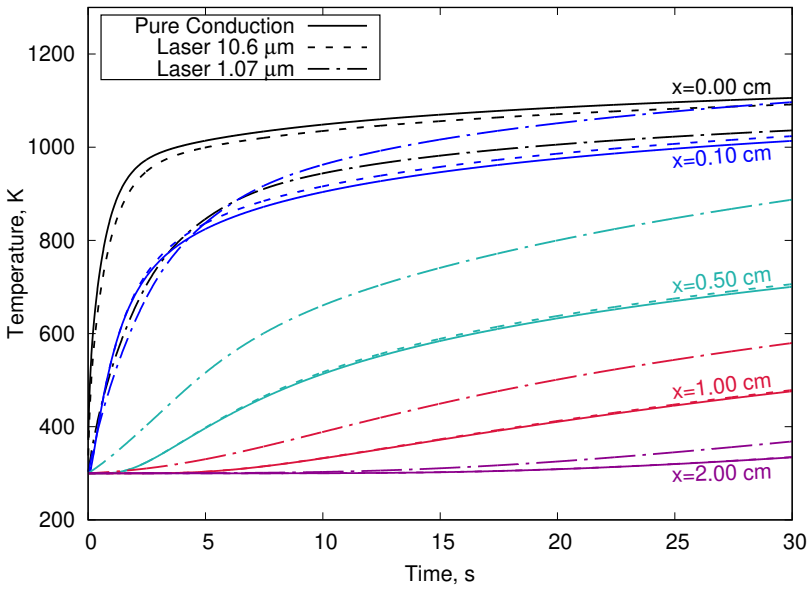

(a) Temperature histories at various locations within the sample

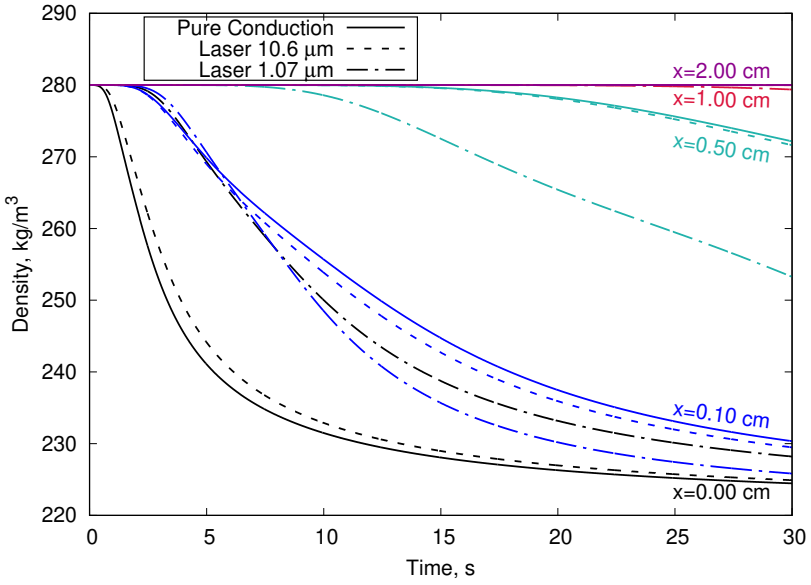

(b) Density histories at various locations within the sample

Fig. 16 Temperature and solid density histories as a function of laser heating time

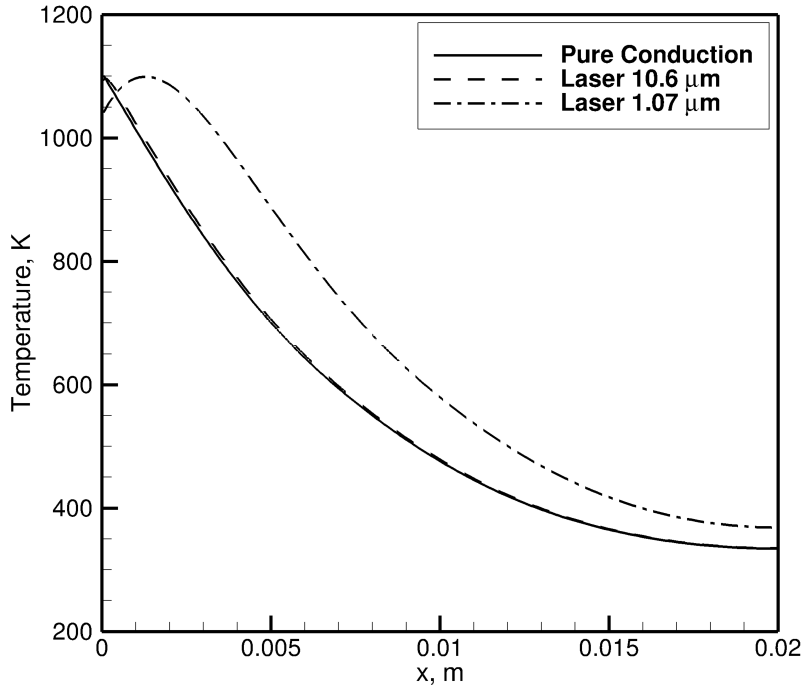

(a) Temperature profiles at various locations within the sample

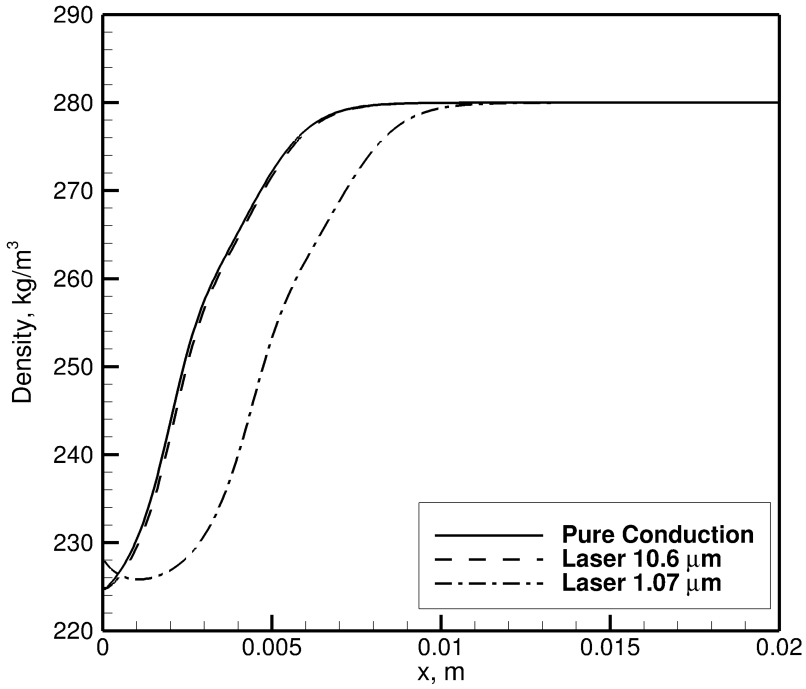

(b) Density profiles at various locations within the sample

Fig. 17 Temperature and solid density profiles along the sample at the end of laser heating time

Table 10 Optical properties of LI-900 based for various lasers

Laser	Wavelength (λ), μm	($\kappa_\lambda, \beta_\lambda$), cm^{-1}
Hydrogen	0.123	(99.00, 177.40)
Argon Ion	0.5145	(0.1627, 59.83)
Fiber	1.07	(0.1211, 69.85)
CO	5.5	(9.5520, 45.91)
CO_2	10.6	(15.18, 233.20)

absorbed is within a thin layer from the heating surface when irradiated by the CO_2 laser, whereas the deposition of the energy goes deeper when irradiated by Fiber laser as expected. These simulation results confirm the behavior observed from the experimental results.

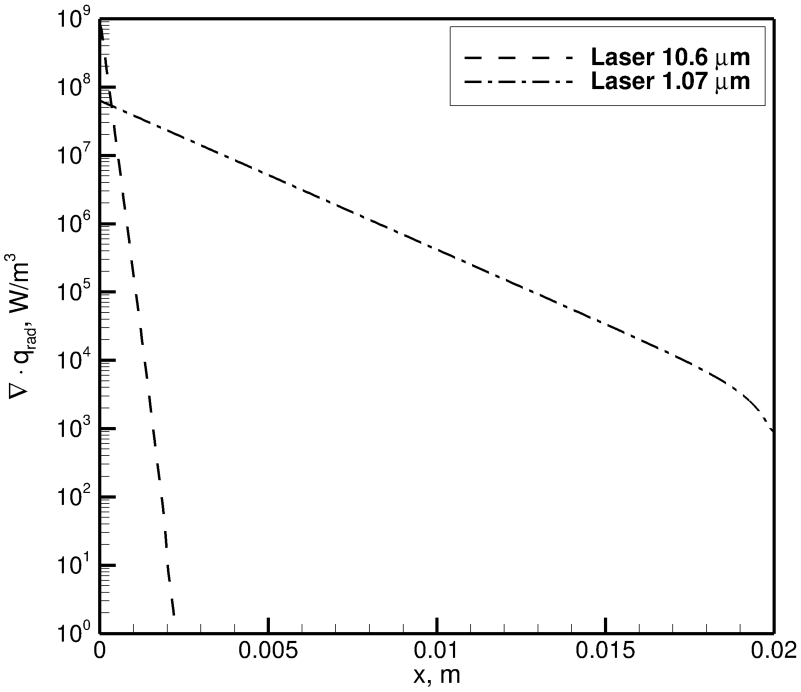

Fig. 18 Radiation source term for two laser simulations along the sample at the end of laser heating time

B. Role of the absorption coefficient

The extent to which the energy gets absorbed within the material is depicted in Fig. 18. It can be observed that the laser travels through the material until its energy is totally absorbed. The region between the heating surface and the location at which the energy is totally absorbed (or the end of the sample in case the energy is not totally absorbed) appears as a layer. In order to investigate this phenomenon further, known laser wavelengths, as given in Table 10, are used, and the simulations are run. Figure 19 shows the results of the simulations. It can be seen that the thickness of the layer in which energy is absorbed within the material is inversely proportional to the absorption coefficient. It is interesting to note that the wavelength of the laser dictates the thickness of the layer through which energy will be

absorbed within the material.

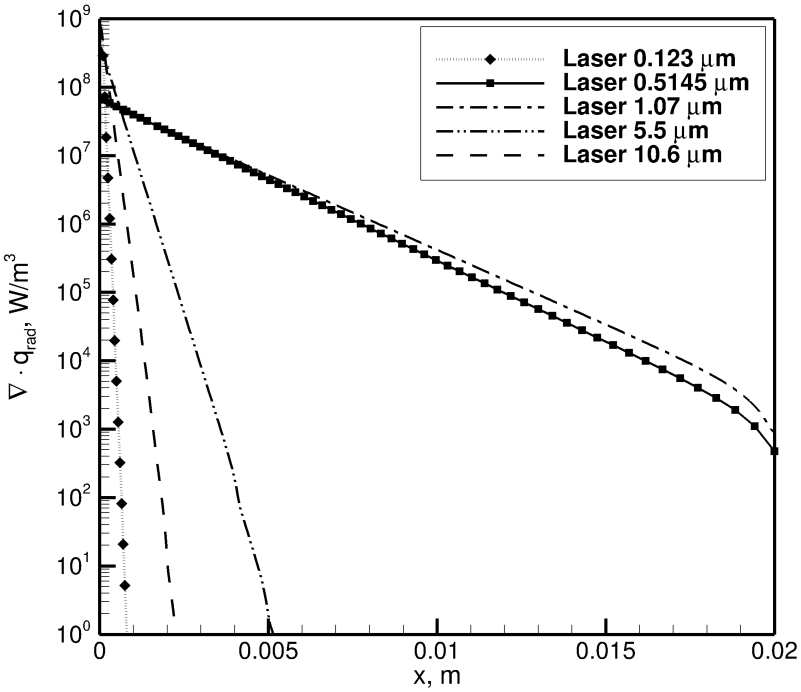

Fig. 19 Radiation source term for different types lasers along the sample at the end of laser heating time

In order to understand the role of the absorption coefficient in more detail, the current optical properties of LI-900 were multiplied by 100, and the simulations were run for both Fiber and CO_2 laser wavelengths. It can be seen from Fig. 20 that the temperature histories when irradiated by Fiber and CO_2 lasers match each other and follow the pure conduction with a minute difference. With high absorption coefficients, the energy is consumed within a thin layer at the surface. The same behavior can be observed for low absorption coefficients where the energy is deposited deep inside instead of at the surface.

V. Conclusion

A coupling scheme between the material response code KATS-MR and a radiative transfer equation (RTE) solver was constructed to study the effects of radiation transport within ablative materials. A P-1 approximation model is used to compute RTE. Verification of RTE was performed by comparing the numerical result with an analytical solution. The verification of the coupling scheme was performed by comparing the temperature histories of pure conduction simulation with conduction-coupled radiative emission simulation. The cases considered for verification study are Marschall et al. cases, 3D Block, 2D IsoQ sample, and the Stardust entry capsule. The predicted temperatures between the two methods show good agreement, with the difference mainly occurring due to high-temperature gradients. Laser ablation simulations were run mimicking the White [7] experiment, and the response of the material to laser heating was studied. The simulation results confirm the behavior noticed from the White [7] experiments.

The results from the verification study indicated that the thermal response could be simulated accurately with the coupling scheme. The verification conducted on multidimensional meshes implies the high robustness of the coupling scheme. The laser ablation simulations numerically confirm the experimental observations of White [7] and conclude that the spectral radiative heat flux could impact the material response of fibrous materials that have low spectral absorption coefficients at the corresponding wavelength. In light of the results obtained with the efficient coupling scheme presented here, the next step is to study the impact of shock layer radiation on the material response.

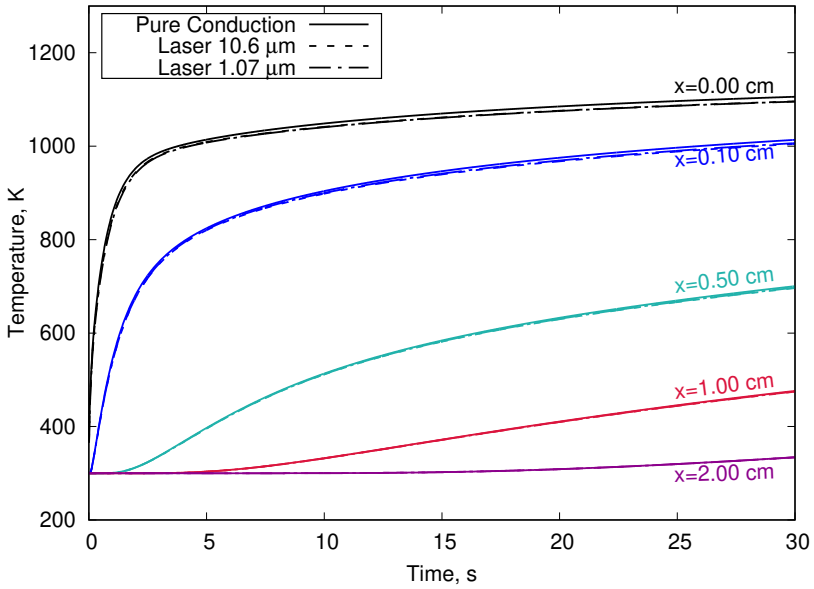

Fig. 20 Temperature histories for simulations with modified optical properties as a function of laser heating time

VI. Acknowledgements

Financial support for this work was provided by the NASA SpaceTech - REDDI - 2018 - ESI grant 80NSSC19K0218. The authors would also like to thank the University of Kentucky Center for Computational Sciences and Information Technology Services Research Computing for their support and use of the Lipscomb Compute Cluster and associated research computing resources. The first author would also like to thank Mr. Scott Fowler (Tecplot, Inc.) for assisting with images and animations.

References

[1] Bowman, W. H., and Lawrence, R. M., "Space Resource. Ablative materials for high-temperature thermal protection of space vehicles," *Journal of Chemical Education*, Vol. 48, No. 10, 1971, p. 690. doi:10.1021/ed048p690.

[2] Lee, S.-C., and George R. Cunnington, J., "Theoretical Models for Radiative Transfer in Fibrous Media," *Annual Review of Heat Transfer*, Vol. 9, 1998, pp. 159–218. doi:10.1615/AnnualRevHeatTransfer.v9.50.

[3] Duffa, G., *Ablative Thermal Protection Systems Modeling*, ISBN 978 1 62410 171 7, American Institute of Aeronautics and Astronautics, 2013. doi:10.2514/4.101717.

[4] Stackpoole, M., Sepka, S., Cozmuta, I., and Kontinos, D., "Post-Flight Evaluation of Stardust Sample Return Capsule Forebody Heatshield Material," *46th AIAA Aerospace Sciences Meeting and Exhibit*, American Institute of Aeronautics and Astronautics, Reno, Nevada, 2008. doi:10.2514/6.2008-1202.

[5] Lachaud, J., Magin, T. E., Cozmuta, I., and Mansour, N. N., "A short review of ablative-material response models and simulation tools," *7th Aerothermodynamics Symposium*, Brugge, Belgium, 2011. doi:2060/20110014340.

[6] White, S., "Solar Tower Radiation Testing of Phenolic Impregnated Carbon Ablator," *Journal of Spacecraft and Rockets*, Vol. 49, No. 5, 2012, pp. 889–893. doi:10.2514/1.A32104.

[7] White, S., "Effects of Laser Wavelength on Ablator Testing," *38th Annual Conference on Composites, Materials and Structures*, Cocoa Beach, Florida, 2014. doi:2060/20140011553.

[8] Bose, D., McCorkle, E., Thompson, C., Bogdanoff, D., Prabhu, D., Allen, G., and Grinstead, J., "Analysis and Model Validation of Shock Layer Radiation in Air," *46th AIAA Aerospace Sciences Meeting and Exhibit*, Reno, Nevada, 2008. doi:10.2514/6.2008-1246.

[9] Modest, M. F., *Radiative Heat Transfer*, 2nd ed., ISBN 978 0 12 503163 9, Academic Press, 2003. doi:10.1016/B978-0-12-503163-9.X5000-0.

[10] Martin, A., and Panesi, M., "Radiative transmission and absorption within the thermal protection system of atmospheric entry spacecraft," *Journal of Spacecraft and Rockets*, Vol. 59, No. 1, 2022, pp. 348–352. doi:10.2514/1.A35029.

[11] Weng, H., and Martin, A., "Multidimensional Modeling of Pyrolysis Gas Transport Inside Charring Ablative Materials," *Journal of Thermophysics and Heat Transfer*, Vol. 28, No. 4, 2014, pp. 583–597. doi:10.2514/1.T4434.

[12] Davuluri, R. S. C., Zhang, H., and Martin, A., "Numerical Study of Spallation Phenomenon in an Arc-Jet Environment," *Journal of Thermophysics and Heat Transfer*, Vol. 30, No. 1, 2016, pp. 32–41. doi:10.2514/1.T4586.

[13] Fu, R., Weng, H., Wenk, J. F., and Martin, A., "Thermomechanical Coupling for Charring Ablators," *Journal of Thermophysics and Heat Transfer*, Vol. 32, No. 2, 2018, pp. 369–379. doi:10.2514/1.T5194.

[14] Balay, S., Gropp, W. D., McInnes, L. C., and Smith, B. F., "Efficient Management of Parallelism in Object Oriented Numerical Software Libraries," *Modern Software Tools in Scientific Computing*, edited by E. Arge, A. M. Bruaset, and H. P. Langtangen, Birkhäuser Press, Boston, MA, 1997, pp. 163–202. doi:10.1007/978-1-4612-1986-6_8.

[15] Balay, S., Brown, J., Buschelman, K., Eijkhout, V., Gropp, W. D., Kaushik, D., Knepley, M. G., McInnes, L. C., Smith, B. F., and Zhang, H., "PETSc Users Manual," Tech. Rep. ANL-95/11 - Revision 3.3, Argonne National Laboratory, 2012.

[16] Balay, S., Abhyankar, S., Adams, M. F., Brown, J., Brune, P., Buschelman, K., Eijkhout, V., Gropp, W. D., Kaushik, D., Knepley, M. G., McInnes, L. C., Rupp, K., Smith, B. F., and Zhang, H., "PETSc Web page," http://www.mcs.anl.gov/petsc, 2014.

[17] Karypis, G., and Kumar, V., "A Fast and High Quality Multilevel Scheme for Partitioning Irregular Graphs," *SIAM Journal on Scientific Computing*, Vol. 20, No. 1, 1998, pp. 359–392. doi:10.1137/S1064827595287997.

[18] Walker, D. W., and Dongarra, J. J., "MPI: a standard message passing interface," *Supercomputer*, Vol. 12, No. 1, 1996, pp. 56–58. URL `https://www.scopus.com/record/display.uri?eid=2-s2.0-0002789358&origin=inward&txGid=b9b115ae3d17f3587282ac510844aea7`.

[19] Weng, H., and Martin, A., "Numerical Investigation of Thermal Response Using Orthotropic Charring Ablative Material," *Journal of Thermophysics and Heat Transfer*, Vol. 29, No. 3, 2015, pp. 429–438. doi:10.2514/1.T4576.

[20] Weng, H., Ümran Düzel, Fu, R., and Martin, A., "Geometric Effects on Charring Ablator: Modeling the Full-Scale Stardust Heat Shield," *Journal of Spacecraft and Rockets*, Vol. 58, No. 2, 2021, pp. 302–315. doi:10.2514/1.A34828.

[21] Ravishankar, M., "Spherical Harmonics based techniques for solution of the Radiative Transfer Equation," Master's thesis, The Ohio State University, Columbus, Ohio, 2009. URL `http://rave.ohiolink.edu/etdc/view?acc_num=osu1243955769`.

[22] Liu, F., Swithenbank, J., and Garbett, E. S., "The boundary condition of the P_N-approximation used to solve the radiative transfer equation," *International Journal of Heat and Mass Transfer*, Vol. 35, No. 8, 1992, pp. 2043–2052. doi:10.1016/0017-9310(92)90205-7.

[23] Eby, S. D., Trepanier, J. Y., and Zhang, X. D., "Modelling radiative transfer in SF_6 circuit-breaker arcs with the P-1 approximation," *Journal of Physics D: Applied Physics*, Vol. 31, No. 13, 1998, pp. 1578–1588. doi:10.1088/0022-3727/31/13/012.

[24] Howell, J. R., Siegel, R., and Menguc, M. P., 5th ed., ISBN 978 0 42 919057 5, CRC Press, Boca Raton, Florida, 2010. doi:https://doi.org/10.1201/9781439894552.

[25] Chen, Y. K., and Milos, F. S., "Ablation and thermal response program for spacecraft heatshield analysis," *Journal of Spacecraft and Rockets*, Vol. 36, No. 3, 1999, pp. 475–483. doi:10.2514/2.3469.

[26] van Eekelen, A. J., and Lachaud, J., "Numerical validation of an effective radiation heat transfer model for fiber preforms," *Journal of Spacecraft and Rockets*, Vol. 48, No. 3, 2011, pp. 534–537. doi:10.2514/1.51865.

[27] Marschall, J., Maddren, J., and Parks, J., "Internal Radiation Transport and Effective Thermal Conductivity of Fibrous Ceramic Insulation," *35th AIAA Thermophysics Conference*, Anaheim, California, 2001. doi:10.2514/6.2001-2822.

[28] Petrov, V. A., "Combined radiation and conduction heat transfer in high temperature fiber thermal insulation," *International Journal of Heat and Mass Transfer*, Vol. 40, No. 9, 1997, pp. 2241–2247. doi:10.1016/S0017-9310(96)00242-6.

[29] Banerji, N., "The effects of radiation on ablative heat shields during atmospheric entry," Ph.d. thesis, Ecole Polytechnique Federale De Lausanne, Lausanne, Switzerland, June 2017. doi:10.5075/epfl-thesis-7681.

[30] Williams, S. D., and Curry, D. M., "Thermal Protection Materials: Thermophysical Property Data," Reference Publication NASA-RP-1289, NASA, Houston, Texas, December 1992. doi:2060/19930009576.

[31] Davuluri, R. S. C., Fu, R., Tagavi, K. A., and Martin, A., "Numerical Investigation on the effect of spectral radiative heat transfer within an ablative material," *AIAA SciTech 2022 Forum*, San Diego, California, 2022. doi:10.2514/6.2022-1283.

[32] Boyd, I. D., Trumble, K. A., and Wright, M. J., "Modeling of Stardust Entry at High Altitude, Part 1: Flowfield Analysis," *Journal of Spacecraft and Rockets*, Vol. 47, No. 5, 2010, pp. 708–717. doi:10.2514/1.37360.

[33] Lachaud, J., van Eekelen, T., Bianchi, D., and Martin, A., "TACOT v3.0," *Ablation Workshop: Code Comparison*, 2014. doi:10.13023/ablation.test.TACOT.